12-8-2017

Hypervelocity Impact of Spherical Aluminum 2017-T4 Projectiles on Aluminum 6061-T6 Multi-Layered Sheets

Michael Deivi Marroquin Salvador

Hypervelocity impact of spherical aluminum 2017-T4 projectiles on aluminum 6061-T6 multi-layered sheets

By

Michael Deivi Marroquin Salvador

A Thesis
Submitted to the Faculty of
Mississippi State University
in Partial Fulfillment of the Requirements
for the Degree of Master of Science
in Aerospace Engineering
in the Bagley College of Engineering

Mississippi State, Mississippi

December 2017

Hypervelocity impact of spherical aluminum 2017-T4 projectiles on aluminum 6061-T6 multi-layered sheets

By

Michael Deivi Marroquin Salvador

Approved:

_____

Thomas E. Lacy
(Major Professor)

_____

Charles U. Pittman Jr.
(Committee Member)

_____

Gregory D. Olsen
(Committee Member)

_____

Santanu Kundu
(Committee Member)

_____

Ratneshwar Jha
(Graduate Coordinator)

_____

Jason M. Keith
Dean
Bagley College of Engineering

Name: Michael Deivi Marroquin Salvador

Date of Degree: December 9, 2017

Institution: Mississippi State University

Major Field: Aerospace Engineering

Major Professor: Dr. Thomas E. Lacy

Title of Study: Hypervelocity impact of spherical aluminum 2017-T4 projectiles on aluminum 6061-T6 multi-layered sheets

Pages in Study 50

Candidate for Degree of Master of Science

With the growing threat of orbital debris impacts to space structures, the development of space shielding concepts has been a critical research topic. In this study, numerical simulations of the hypervelocity impact response of stacked aluminum 6061-T6 sheets were performed to assess the effects of layering on penetration resistance. This work was initially motivated by set of experimental tests where a stack of four aluminum sheets of equal thickness was observed to have a higher hypervelocity ballistic resistance than a monolithic aluminum sheet with the same total thickness. A set of smoothed particle hydrodynamic simulations predicted a 40% increase in the ballistic limit for a 6-layer target compared to a monolithic sheet. In addition, the effect of variable sheet thickness and sheet ordering on the impact resistance was investigated, while still maintaining a constant overall thickness. A set of thin layers in front of a thick layer generally lead to a higher predicted ballistic limit than the inverse configuration. This work demonstrates an increase in the performance of advanced space shielding structures associated with multi-layering. This suggests that it may be possible to dramatically improve the performance of such structures by tailoring the material properties, interfaces, and layering concepts.

DEDICATION

To my mom and step-dad for their support in my education.

Thank You,

Michael Salvador

ACKNOWLEDGEMENTS

I want to express my deepest appreciation and thanks to Dr. Thomas E. Lacy Jr. for his support and guidance throughout this research. It has been an honor to have him as my advisor and professor. And I am grateful for the opportunity of this challenging and enjoyable road to the completion of this thesis and I know it would have not been possible without him.

I also want to give my sincerest gratitude and thanks to Dr. Charles U. Pittman Jr. for his valuable suggestions and comments that proved valuable in the achievement of this thesis as well as the rest of my committee members Dr. Gregory Olsen and Dr. Santanu Kundu.

I take this opportunity and give thanks to Hunter Bowering, Kalyan Kota and Patrick Irizarry for their advice throughout this work and help in the operation of laboratory equipment. Also, I want to express thanks to all of my research colleagues for their constructive comments during our research meetings.

And I thank all of my family and friends for their support and encouragement throughout the achievement of this thesis.

TABLE OF CONTENTS

DEDICATION ii

ACKNOWLEDGEMENTS iii

LIST OF TABLES vi

LIST OF FIGURES vii

CHAPTER

I. INTRODUCTION 1

1.1 Growing Orbital Debris Threat and Space Shielding Methods 1

II. EXPERIMENTAL AND NUMERICAL STUDY OF MULTI-LAYERED ALUMINUM SHEETS 5

2.1 Abstract 5
2.2 Introduction 6
2.3 Preliminary HVI Tests 11
2.3.2 Method 12
2.3.3 HVI Experimental Results 14
2.4 Smoothed Particle Hydrodynamics Estimates of V50 17
2.4.1 Material Model and Equation of State 18
2.4.2 Axisymmetric SPH Models of HVIs to 6061-T6 Monolithic and Layered Targets 21
2.4.3 SPHC Validation 22
2.4.4 SPHC Simulations of HVIs to Monolithic and Layered 6061-T6 Targets 26
2.4.4.2 Parametric Study of the Ballistic Limit of Multi-Layered Targets 29
2.4.4.3 Effect of Variable Target Layer Thicknesses on Penetration Resistance 35
2.5 Conclusions 41

III. CONCLUSIONS AND FUTURE WORK 43

3.1 Conclusions 43
3.2 Future Work 45

REFERENCES 46

LIST OF TABLES

2.1 Calculated Velocities of the Aluminum Projectiles 14

2.2 Johnson-Cook Material Constants for Projectile and Targets.....19

2.3 EOS Parameters for Projectile and Target Sheets 21

2.4 Measured [40] and Predicted [40] Hypervelocity Impact Damage to a ASTM A36 Steel Plate due to Plastic Cylinders at a 5.036 km/s Velocity.....26

LIST OF FIGURES

1.1 Number of orbital debris cataloged by NASA since 1961 [2]. 2

1.2 Orbital debris impact damage on space shuttle radiator [5]. 3

2.1 Whipple Shield method [9]. 7

2.2 The ballistic limit comparison between a monolithic shield and Whipple Shield. The monolithic shield is composed of single Al 6061-T6 sheet with 0.44 cm thickness and Whipple Shield is an Al 6061-T6 bumper and rear wall with 0.12 cm and 0.32 cm thickness respectively. The standoff distance of the Whipple Shield is 10 cm [9]. 8

2.3 4-layered target configuration with a witness sheet located 5 cm behind the layered target. 12

2.4 a) Mississippi State University two stage light gas gun, b) 2D schematic of major components (from [23]). 13

2.5 Projectile and sabot impact damage at the impact surface (left) and back surface (right) of the monolithic aluminum 6061-T6 sheet. The M4 monolithic sheet was impacted by a 1 mm diameter Al 2017-T4 spherical projectile at a velocity of 5.04 km/s. Backlight was visible through both sides of HVI crater. 15

2.6 Projectile and sabot impact damage at the impact surface (left) and back surface (right) of the four-layer Al 6061-T6 target. The L4 target was impacted by a 1 mm diameter Al 2017-T4 spherical projectile at a velocity of 5.04 km/s. 16

2.7 Evidence of debris cloud between first (left) and second (right) layer of the four-layer Al 6061-T6 target. The L4 target was impacted by a 1 mm diameter Al 2017-T4 spherical projectile at a velocity of 5.04 km/s. 17

2.8 SPHC models of a) monolithic target and b) 4-layer target. Projectile and target sheet materials are Al 2017-T4 and Al 6061-T6, respectively. 22

2.9 HVI response of a 1.5 mm thick Al 6061-T6 sheet 7.2 μs after a 7.6 km/s impact with an Al 2017-T4 projectile; a) Measured radiographic image from [38], b) AUTODYN 2D axisymmetric SPH prediction from [39], and c) 2D axisymmetric SPHC prediction performed in this study. 23

2.10 2D SPHC model of a cylindrical Nylon-6 projectile and ASTM A36 steel target plate. 24

2.11 HVI damage to a 12.7 mm thick ASTM A36 steel plate due to a 5.6 mm diameter x 8.6 mm Lexan (a, b, and c) or Nylon-6 (d) cylindrical projectile at 5.063 km/s. a) Experimental results from [40]; LS-DYNA (b) and CTH (c) predictions of damage 10 μs after impact from [40]; and SPHC prediction of damage 10 μs after impact in this study. 25

2.12 HVI response of (left) an Al 6061-T6 monolithic sheet (total thickness, 0.254 cm) and (right) 4-layer target (sheet thickness, 0.254 cm/4 = 0.0635 cm) subjected to 1.4 km/s Al 2017-T4 projectile impacts at a) 0 μs, b) 10 μs c) 20 μs and d) 30 μs after impact. 28

2.13 Ballistic limit (V50) upon increasing particle density (50k, 100k, 200k, 300k, 400k, and 500k) for the Al 6061-T6 monolithic target and the 2-, 4-, 6-, and 8-layer targets subjected to 1 mm diameter Al 2017-T4 projectiles. A constant total thickness 0.254 cm was held on all predicted V50 simulations. 30

2.14 Ballistic limit (V50) upon increasing the number of Al 6061-T6 target layers subjected to 1 mm diameter Al 2017-T4 projectile impacts. The predicted V50 was performed using 50k, 100k, 200k, 300k, 400k and 500k total particles. 32

2.15 Normalized ballistic limit ($V50/V50_m$) upon increasing number of equally thick layers at constant total thickness of 0.254 cm. In all predicted V50 simulations, an Al 2017-T4 projectile impacted an Al 6061-T6 target. Overestimated V50 is shown past the vertical dash line; downward arrows indicate the V50 to be lower than what is shown. 33

2.16 Comparison of Al 6061-T6 a) 4-layer target to b) 16-layer target subjected to a 1 mm diameter Al 2017-T4 projectile HVI of 1.4 km/s at 10 μs after impact. A total target thickness of 0.254 cm was used for both simulations. 35

2.17 SPHC models for a) [$(¼)_2$ / ½] and b) [½ / $(¼)_2$] target configurations. Projectile and target sheet materials are Al 2017-T4 and Al 6061-T6, respectively. 36

2.18 Predicted HVI response of Al 6061-T6 a) [(¼)$_2$ / ½], b) [½ / (¼)$_2$] and c) monolithic sheet target subjected to 1 mm diameter 2017-T4 projectile HVI of 1.4 km/s at 10 μs after impact. A constant target total thickness of 0.254 cm was held in all three simulations. 37

2.19 Predicted HVI response of Al 6061-T6 a) [(¼)$_2$ / ½], b) [½ / (¼)$_2$] and c) 4-layer target subjected to 1 mm diameter 2017-T4 projectile HVI of 1.6 km/s at 10 μs after impact. A constant target total thickness of 0.254 cm was held in all three simulations. 39

2.20 HVI impact response of Al 6061-T6 [(1/8)$_4$ / ½] target subjected to 1 mm diameter Al 2017-T4 projectile at a HVI of 1.60 km/s at 10 μs after impact with a total thickness of 0.254 cm. 40

2.21 Normalized ballistic limit (V50/V50$_m$) comparison between multi-layer targets of equally thick layers versus targets of varying layer thickness. For all predicted V50 simulations, a 1 mm diameter Al 2017-T4 projectile impacted an Al 6061-T6 target with a total thickness of 0.254 cm.....41

CHAPTER I

INTRODUCTION

1.1 Growing Orbital Debris Threat and Space Shielding Methods

There are numerous obstacles that exist for space explorations; some of them occur in near-Earth orbits. One of the many concerns are micrometeoroids and orbital debris (MMOD). Due to many past space launches, accumulations of MMOD present in the near-Earth orbit commonly impact satellites or spacecraft at velocities of 8 km/s or higher. Even though the National Aeronautics and Space Administration (NASA) and the Department of Defense (DoD) are tracking those debris, they can only track particles with nominal diameters of 10 cm or larger; smaller debris are very difficult to track or avoid [1]. A plot of the orbital debris cataloged by NASA since 1961 is shown in Figure 1.1 [2]. The amount of orbital debris significantly increased over the years, including dramatic jumps in 2007 and 2009 due to the Fengyun Anti-Satellite Test [3] and the Iridium-Cosmos Collision [4], respectively. A total of 17,876 pieces of orbital debris 10 cm or larger have been tracked and catalogued. However, an estimated 500,000 fragments of orbital debris between 1-10 cm and millions of fragments smaller than 1 cm reside in the near-Earth environment [1].

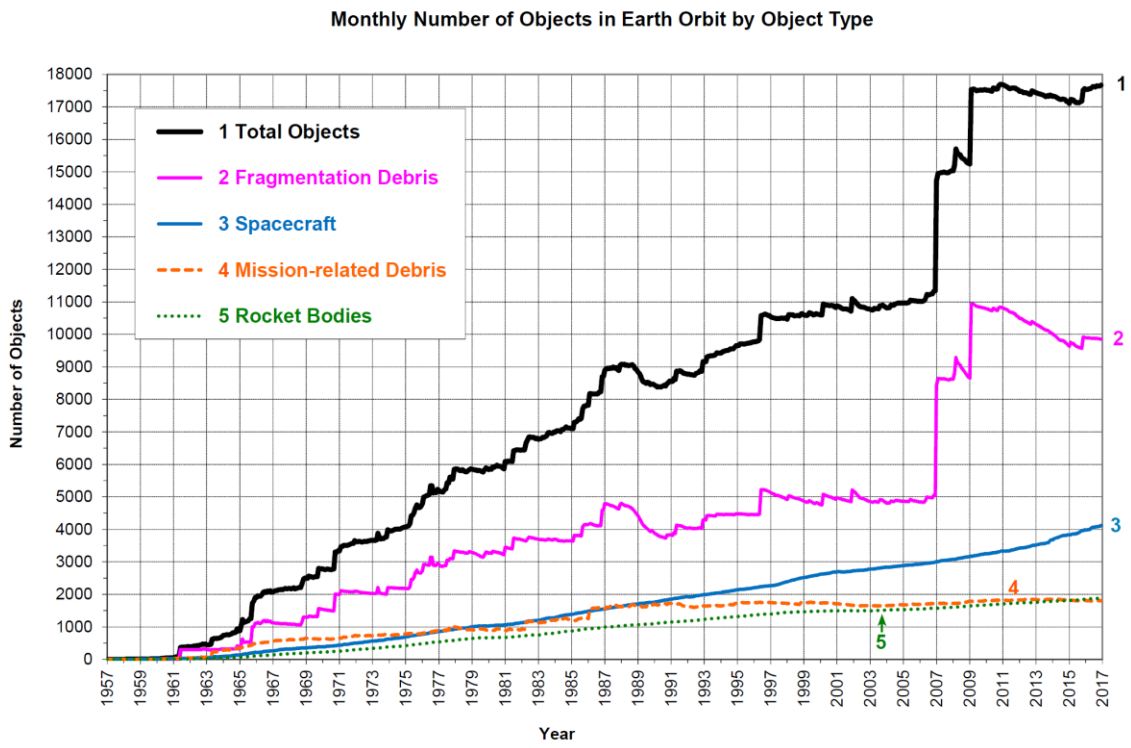

Figure 1.1 Number of orbital debris cataloged by NASA since 1961 [2].

The continuous growth in the amount of orbital debris and undetectable fragments causes major concerns for satellites and spacecraft. Figure 1.2 shows orbital debris impact damage on a space shuttle radiator [5]. Similar orbital debris impacts to space shuttles, the International Space Station (ISS), and satellites are common; resulting in expensive repairs or replacements to critical space structures and components. Due to this growing threat, the development of space shielding structural concepts necessary to protect spacecraft and satellites from orbital debris impacts has become an increasing priority. Originally, a sacrificial monolithic shield (offset metallic wall) was used to protect spacecraft from MMOD, but now more advanced shielding methods are being applied. Historically, two of the most commonly used space shielding methods are the Whipple Shield proposed by Fred Whipple in 1947 [6] and the Stuffed Whipple Shield

developed by a team composed by the Marshall Space Flight Center (MSFC) and Johnson Space Center (JSC) in 1995 [7] (a detail description of these shielding methods will be discussed in Chapter II). These two methods are currently used on the ISS to protect its vital structures with larger surface areas from orbital debris impacts during long periods of exposure [8].

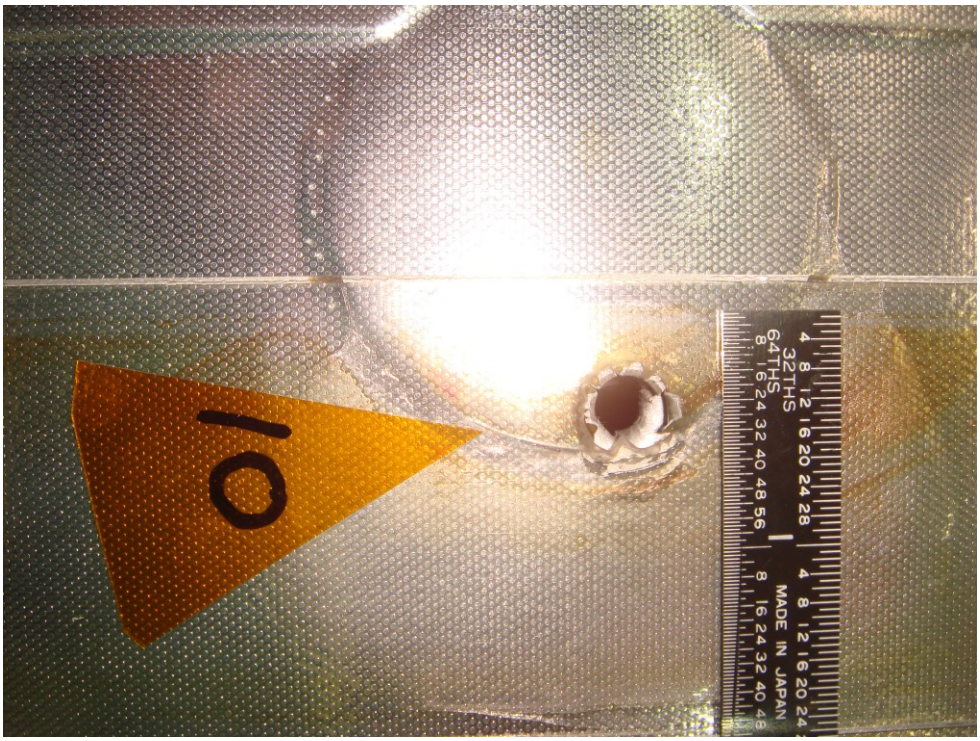

Figure 1.2 Orbital debris impact damage on space shuttle radiator [5].

These shielding methods [6, 7] have proven to increase the protection of spacecraft structures from the threat of space debris. Nevertheless, extensive research has been conducted to improve the efficiency of space shielding. In this paper, a comparative study was conducted to compare the hypervelocity impact (HVI) behavior of a monolithic aluminum sheet with that for different arrangements of stacked aluminum sheets with the same overall mass and thickness. The focus of this study was to assess the

effect of layering on the HVI ballistic resistance of aluminum targets with the same overall weight and thicknesses.

A two-stage light gas gun (2SLGG) at Mississippi State University (MSU) was used to perform several experimental tests to simulate space debris HVIs on a 0.254 cm thick monolithic aluminum sheet and a stack of four 0.0635 cm thick aluminum sheets. The 2SLGG is capable of propelling projectiles up to 7 km/s, consistent with space debris impacts. However, only a limited number of experimental tests were performed due to the high cost of each test, difficulties in obtaining accurate projectile velocity measurements, and other issues. Therefore, a Smooth Particle Hydrodynamic Code (SPHC) was used to simulate HVIs involving a wide range of projectile velocities and layered aluminum targets. This work is summarized in Chapter II of this thesis. In Chapter III, an overall conclusion of the study and a discussion of future work is presented.

CHAPTER II

EXPERIMENTAL AND NUMERICAL STUDY OF MULTI-LAYERED ALUMINUM SHEETS

2.1 Abstract

With the growing threat of orbital debris impacts to space structures, the development of space shielding concepts has been a critical research topic. In this study, numerical simulations of the hypervelocity impact response of stacked aluminum 6061-T6 sheets were performed to assess the effects of layering on penetration resistance. This work was initially motivated by set of experimental tests where a stack of four aluminum sheets of equal thickness was observed to have a higher hypervelocity ballistic resistance than a monolithic aluminum sheet with the same total thickness. A set of smoothed particle hydrodynamic simulations predicted a 40% increase in the ballistic limit for a 6-layer target compared to a monolithic sheet. In addition, the effect of variable sheet thickness and sheet ordering on the impact resistance was investigated, while still maintaining a constant overall thickness. A set of thin layers in front of a thick layer generally lead to a higher predicted ballistic limit than the inverse configuration. This work demonstrates an increase in the performance of advanced space shielding structures associated with multi-layering. This suggests that it may be possible to dramatically improve the performance of such structures by tailoring the material properties, interfaces, and layering concepts.

2.2 Introduction

Space shielding against micrometeoroids and orbital debris (MMOD) has become an increasing priority within the last decade due to an increase in debris associated with China's anti-satellite test [3] and the collision between two intact satellites [4]. Historically, a sacrificial monolithic shield was initially used to protect spacecraft from MMOD. However, more advanced shielding methods like the Whipple Shield [6] or Stuffed Whipple Shield [7] are now being applied. A typical monolithic shield can be made of a 0.44 cm thick aluminum 6061-T6 wall while a Whipple Shield is comprised of a thin 0.12 cm sacrificial aluminum 6061-T6 wall "bumper" distanced by 10 cm from a thicker 0.32 cm wall [9]. During hypervelocity impact (HVI) of a monolithic shield, there are no advanced methods used to dissipate the initial impact energy. The monolithic shield must absorb the full HVI energy of the projectile. As for a Whipple Shield, the orbital debris impacts the exterior bumper wall where the orbital debris and part of the bumper are broken into small fragments described as a "debris cloud." Due to the initial impact and fragmentation, the total kinetic energy in the debris cloud is significantly lower than that for the incoming MMOD, decreasing the impact damage on the interior wall (critical structure). The Whipple Shield concept is shown schematically in Figure 2.1 [9], where the "rear wall" corresponds to a spacecraft hull or critical structure. Ideally, the bumper sheet and standoff distance will promote debris cloud expansion that minimizes the likelihood of severe damage (craters, holes, spallation) to the rear wall structure. Figure 2.2 [9] shows the comparison of the ballistic limit (velocity at which a particular projectile reliably penetrates a particular material at least 50% of the time) between the monolithic shield and Whipple Shield; each shield was impacted by an

aluminum sphere of varying diameters. The impacts occurred orthogonal (normal) to the targets. The ballistic limit of the Whipple Shield (solid line) is larger than the monolithic shield (dotted line) at impact velocities higher than 3 km/s. The Whipple Shield ballistic limit largely increases due to the standoff distance between the bumper wall and rear wall. Of course, the results depend on the thickness of the target, standoff distance and projectile characteristics.

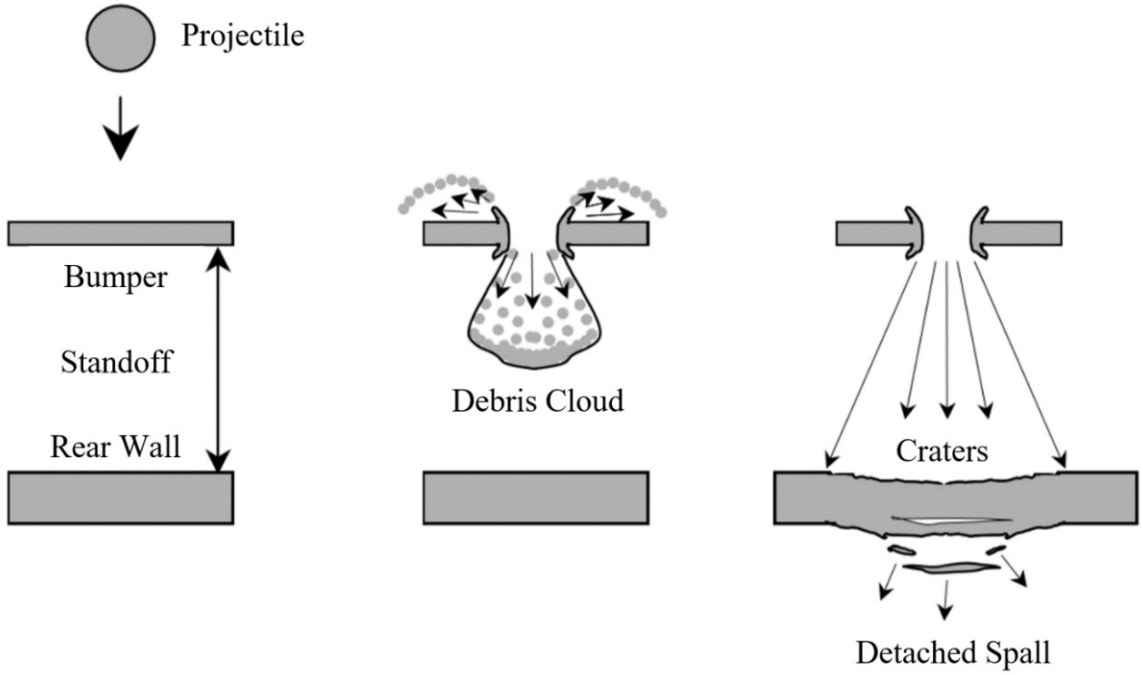

Figure 2.1 Whipple Shield method [9].

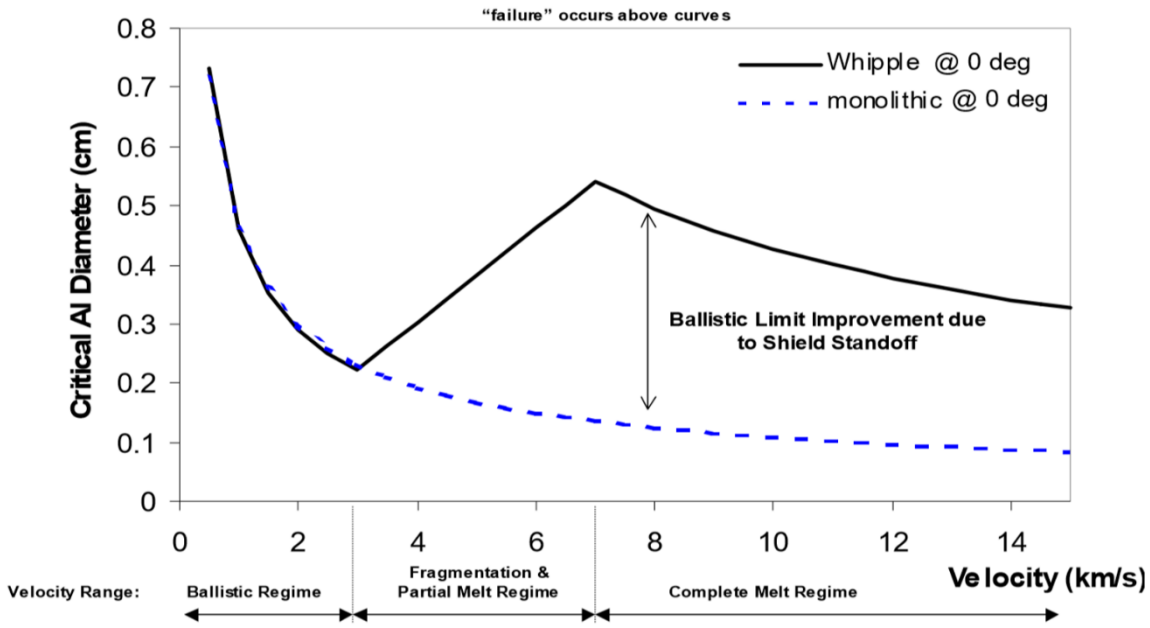

Figure 2.2 The ballistic limit comparison between a monolithic shield and Whipple Shield. The monolithic shield is composed of single Al 6061-T6 sheet with 0.44 cm thickness and Whipple Shield is an Al 6061-T6 bumper and rear wall with 0.12 cm and 0.32 cm thickness respectively. The standoff distance of the Whipple Shield is 10 cm [9].

Similarly, a Stuffed Whipple Shield is composed of a bumper and offset rear wall sandwiched around a Nextel/Kevlar layer (equally spaced between the bumper and rear wall). Christiansen et al. [7] showed a Stuffed Whipple Shield stopped 50%-300% larger projectiles than an aluminum double bumper shield with equal mass (i.e., Stuffed Whipple where the Nextel/Kevlar layer is replaced with another aluminum bumper wall). By comparing with previously published data on Whipple shields [10], Christiansen et al. [7] indicated that a Stuffed Whipple Shield weighing 2.5 times less than a Whipple Shield would stop a 1.35 cm diameter projectile at an impact velocity of 7 km/s with a standoff distance of 11 cm. Another advantage of a Stuffed Whipple Shield is the greater protection at short standoff distances (i.e., when the ratio between the standoff distance and the projectile diameter is less than 15) than a Whipple [6], Mesh Double-Bumper

[11]or Multi-Shock [12] Shield. A shorter standoff distance would allow a decrease in the exterior volume of a spacecraft structure or an increase in the usable payload volume for a given set of exterior dimensions.

These shielding methods [6, 7, 11, 12] have proven to greatly reduce the impact damage compared to a monolithic shield by dissipating the initial kinetic energy through fragmentation of MMOD. However, little research has been performed to optimize a monolithic shield, or rear wall of a Whipple Shield by subdividing the monolithic wall into a stack of layered sheets adjacent to each other while maintaining essentially the same overall thickness. While some published research exists for layered targets subjected to projectile velocities ranging from 200-1000 m/s [13-20], little similar work has been performed at hypervelocities greater than 1 km/s.

Teng et al. [13] developed explicit finite element simulations of ballistic impacts to a monolithic Weldox 460 E steel shield and double-layered shields of the same material for four different projectiles at impact velocities of 285 m/s, 317 m/s, and 600 m/s. The double-layered shield increased the predicted ballistic limit (V50, i.e., velocity at which a particular projectile penetrates a particular target at least 50% of the time) by 8-25% for cylindrical projectiles. These predictions [13] were in good agreement with LS-DYNA [14] simulations and experimental results of Dey et al. [15] and Børvik et al. [16] on double-layered shields. Also, Teng et al. [13] showed that introducing small gap spacing between the plates while still permitting layer contact during impact has little effect on the ballistic limit.

Similarly, Marom and Bodner [17] demonstrated experimentally that four stacked layers of aluminum 6061-T6 (layer thickness, 1 mm) exhibited a higher ballistic

resistance than an aluminum 6061-T6 monolithic target plate of 3.6 mm thickness at projectile velocities averaging 375 m/s. Although the total thicknesses of the two targets differed by 0.4 mm, the four-layer target was approximately 50% more effective at decreasing the initial projectile velocity than the monolithic plate. The experimental study was performed for a range of increasing layer thicknesses and numbers of layers (1-10) in a target. A simple analytical model was developed and compared to the experimental results. They concluded that the increase in the ballistic resistance of the stacked layers was due to the deformation of the layers in a target. Gamache et al. [18] conducted an experimental study of an aluminum/polyurea laminate backed with a steel substrate. The ballistic limit varied with increasing number of laminate layers while maintaining the same overall target thickness. However, the highest ballistic limit was obtained at eight bilayers of aluminum/polyurea; the ballistic limit decreased thereafter with increasing number of thinner bilayers.

Other researchers concluded that a multi-layered shield could result in *lower* ballistic resistance than a monolithic shield of equal thickness and mass [19, 20]. The application of multi-layered shields is dependent on the projectile shape mass and geometry, impact velocity, ratio of projectile diameter to target thickness, projectile and target material properties, layering geometry, and other factors [21] . The work summarized in [13, 15, 16, 17, 18, 19] involved lower projectile velocities ranging from 200-1000 m/s; further study is required to assess the effects of multi-layered shields at hypervelocities greater than 1 km/s.

In this study, projectile velocities greater than 1 km/s were used to assess the effects of different layering arrangements of thin 6061-T6 sheets with the same total

stack-up thickness on hypervelocity ballistic resistance. 6061-T6 targets with a total thickness, 0.254 cm, were subjected to simulated impacts with 1 mm diameter spherical 2017-T4 projectiles. The numerical simulations were motivated by a series HVI tests involving stacked aluminum sheets that suggested a four-layered target had a higher ballistic limit (V50) than a monolithic plate with the same total thickness. A parametric study was performed, using Smoothed Particle Hydrodynamic (SPH) simulations, to probe the effects of target layers of varying thicknesses and stacking sequence on predicted V50.

2.3 Preliminary HVI Tests

A set of four HVI experiments were performed for each of two 10.16x10.16x0.254 cm^3 6061-T6 Al target configurations subjected to impacts with a 1mm diameter Al 2017-T4 spherical projectiles. For the first configuration, the targets were monolithic Al sheets (thickness, 0.254 cm). In the second configuration, the targets were assemble using four stacked 0.0635 cm Al sheets (total thickness, 0.254 cm); no adhesive bonding was employed between layers. Each target was bolted at four corners to a witness sheet attached at an offset distance of 5 cm behind the target. Figure 2.3 shows a typical target configuration.

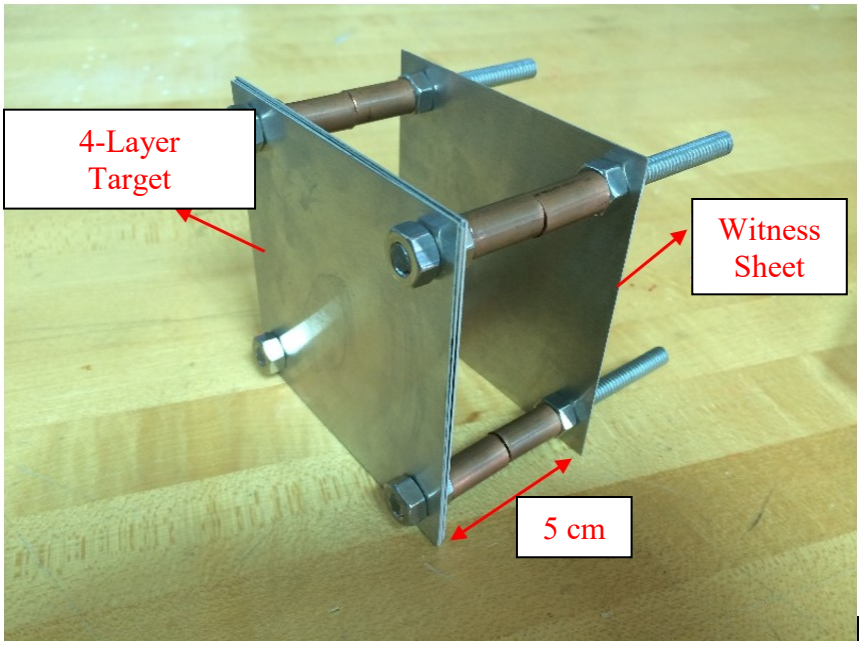

Figure 2.3 4-layered target configuration with a witness sheet located 5 cm behind the layered target.

2.3.2 Method

Mississippi State University's two-stage light gas gun (Figure 2.4a) was used to perform a series of preliminary experimental tests. A typical experiment is performed as follows: a 22-caliber cartridge housing a high-density polyethylene piston was loaded inside the chamber. Once the round is fired, the piston travels inside the pump tube where it compresses helium (light) gas; this is considered to be the first stage of a two-stage light gas gun [22]. The second stage occurs when the piston further compresses the light gas in the acceleration reservoir. A Mylar (polyester film) burst disk is located directly upstream of the sabot (a device to hold and center the projectile inside the barrel) (cf., dashed inset in Figure 2.4b [23]). Once the helium gas is sufficiently compressed, the buildup pressure ruptures the Mylar burst disk and propels the projectile and sabot through the barrel at hypervelocity. As the projectile and sabot exit the barrel and enter

the flight tube, the sabot separates from the projectile and (ideally) strikes a stripper plate positioned at the center of the target chamber; this allows the projectile to hit the designated target.

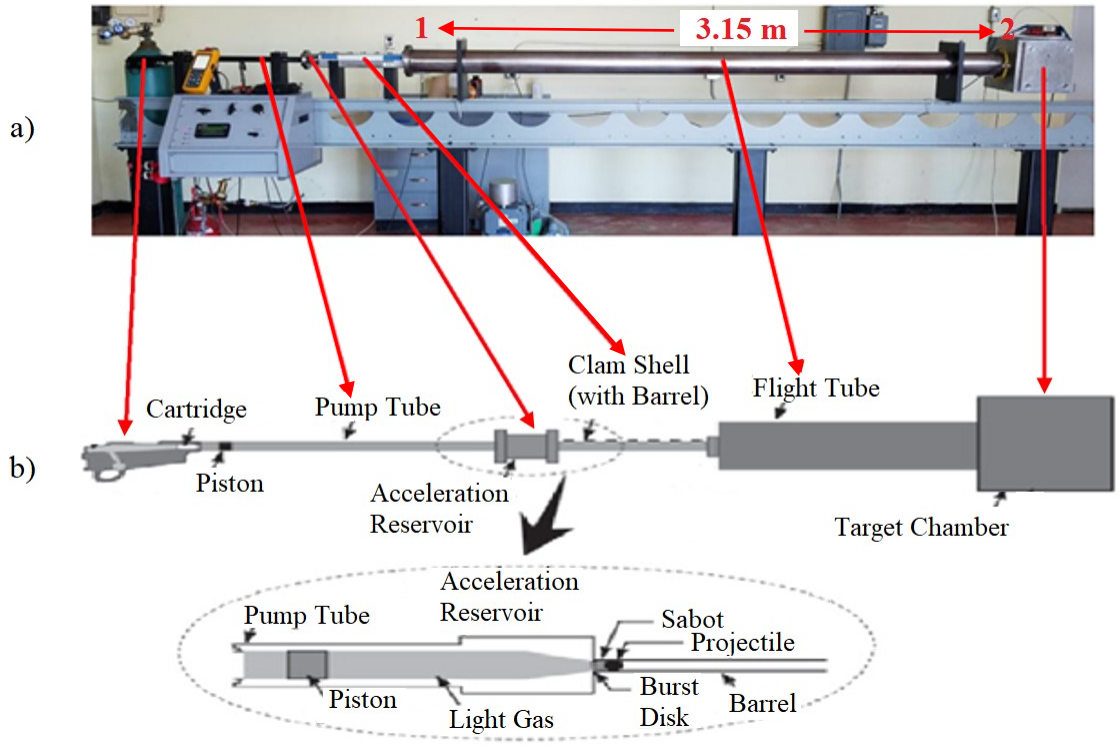

Figure 2.4 a) Mississippi State University two stage light gas gun, b) 2D schematic of major components (from [23]).

Individual targets are attached downstream to the backside of the stripper plate. As the 1 mm diameter Al 2017-T4 projectile and plastic sabot exit the barrel, the sabot separates from the projectile due to a small drag force caused by a low atmospheric pressure in the flight tube. Not all tests resulted in a complete separation between the sabot and projectile, and in some tests the sabot also impacted the target.

Projectile velocities were measured using two photodiodes connected to an oscilloscope. The first photodiode is located at the entrance of the flight tube, and the

second photodiode is positioned at the front face of the target chamber at a distance of 3.15 m from each other (Figure 2.4a). Photodiodes detect emitted light and generate a current as the projectile/sabot exit from the barrel and impact the stripper plate/target. The oscilloscope is set to trigger on these current/voltage spikes. Thus, the projectile flight time can be determined from the time between each voltage spike, and the projectile velocities were determined using the known separation distance between photodiodes.

2.3.3 HVI Experimental Results

A total of eight HVI tests were performed, four using monolithic Al 6061-T6 targets (Tests M1-M4) and four using 4-layer Al 6061-T6 targets (Tests L1-L4). Table 2.1 contains a summary of the time between photodiode measurements, distance between photodiodes, and projectile velocities for each test. In addition, the table indicates whether or not the projectile penetrated a given target. Observations of the impact damage were made for all eight tests.

Table 2.1 Calculated Velocities of the Aluminum Projectiles

Test ID[1]	Time (μs)	Distance Between Photodiodes (m)	Calculated Velocity (km/s)	Target Penetration (Y/N)
M1	880	3.15	3.58	N
M2	784	3.15	4.02	N
M3	680	3.15	4.63	N[2]
M4	624	3.15	5.04	Y
L1	728	3.15	4.32	N
L2	696	3.15	4.52	N
L3	664	3.15	4.86	N
L4	624	3.15	5.04	N

[1]M = monolithic target and L= four-layered target
[2]Visible cracking observed on back face

In tests M1-M2 the projectile did not penetrate the monolithic sheets. For a HVI of 3.58 km/s in test M1, slight bulge was observed on the back surface of the monolithic sheet. A somewhat larger occurred in test M2 at a HVI of 4.02 km/s. At a higher HVI of 4.63 km/s, backface cracking was observed in test M3. A high-intensity backlight was used to visually inspect for through cracks and/or complete penetration. When specimen M3 was held in front of the backlight, no visible light was apparent through the impact site, indicating the target was not perforated. However, for test M4 at a HVI of 5.04 km/s, light was visible through the impact crater (Figure 2.5) as a consequence of complete projectile penetration.

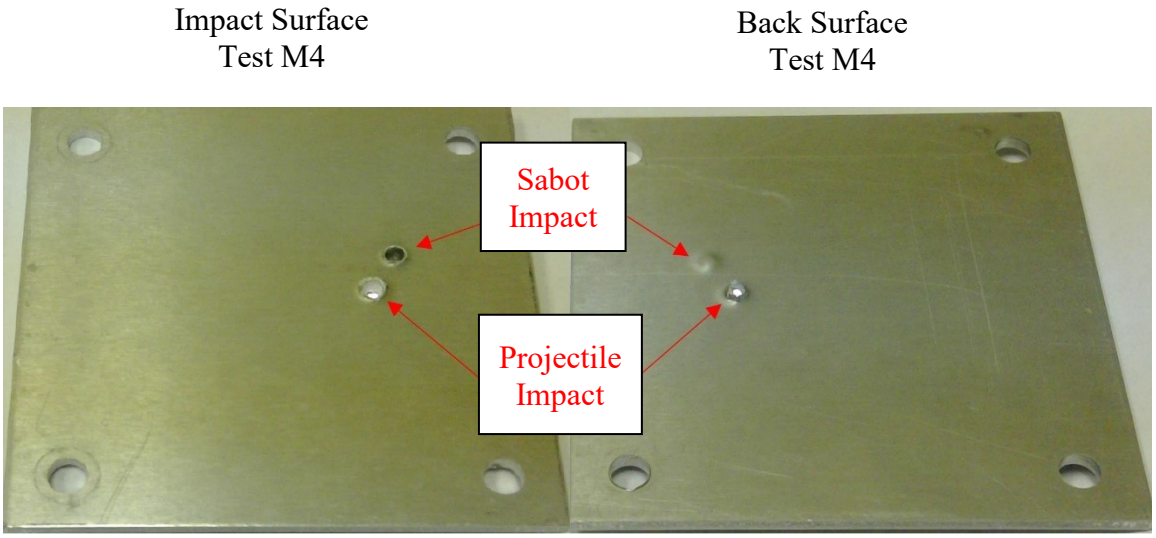

Figure 2.5 Projectile and sabot impact damage at the impact surface (left) and back surface (right) of the monolithic aluminum 6061-T6 sheet. The M4 monolithic sheet was impacted by a 1 mm diameter Al 2017-T4 spherical projectile at a velocity of 5.04 km/s. Backlight was visible through both sides of HVI crater.

For tests L1-L4, the 4-layer targets were not penetrated by the projectiles. For test L1 at a HVI of 4.32 km/s, the projectile penetrated the first layer and formed a dimple/crater in each of the last three layers. The second and third layer were stuck

together, perhaps due to mechanical interference or localized melting/solidification. On the backface of the fourth layer, a bulge was observed but there were no signs of cracking. Tests L2 and L3 at HVIs of 4.52 km/s and 4.86 km/s respectively, showed similar impact damage to that for test L1. The projectile penetrated the first layer and perforated the second sheet; cracking was observed in the second layer of target L3. For test L4 at HVI of 5.04 km/s, the projectile penetrated the first layer and perforated the second similar to test L3. The second, third and fourth layer were stuck together; there was a bulge at the backface of the fourth layer but no signs of cracking/penetration (Figure 2.6). Consistent evidence of debris cloud dispersion between the first and second layers was observed on all tests (L1-L4) after penetration of the first layer (e.g., Figure 2.7).

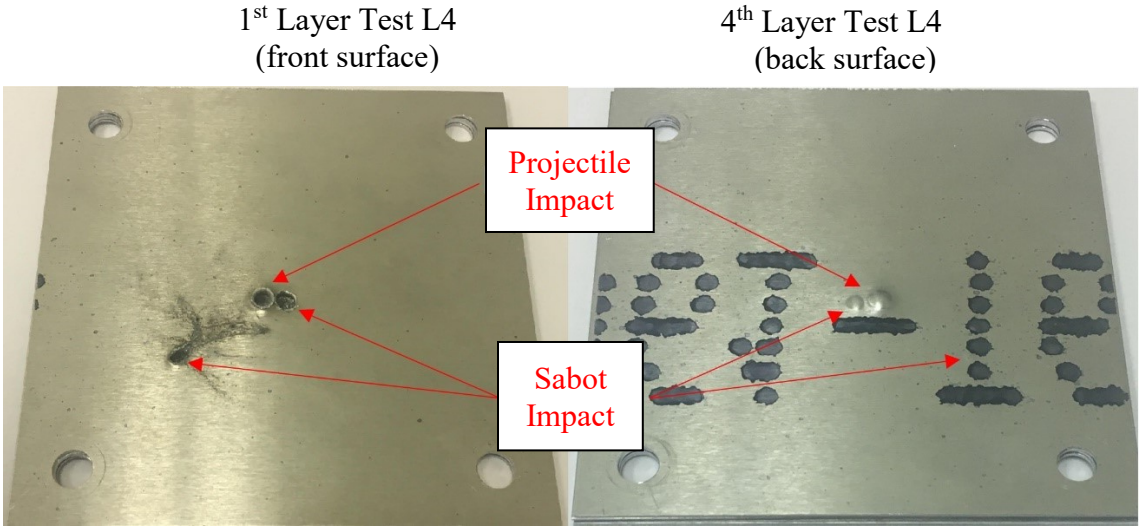

Figure 2.6 Projectile and sabot impact damage at the impact surface (left) and back surface (right) of the four-layer Al 6061-T6 target. The L4 target was impacted by a 1 mm diameter Al 2017-T4 spherical projectile at a velocity of 5.04 km/s.

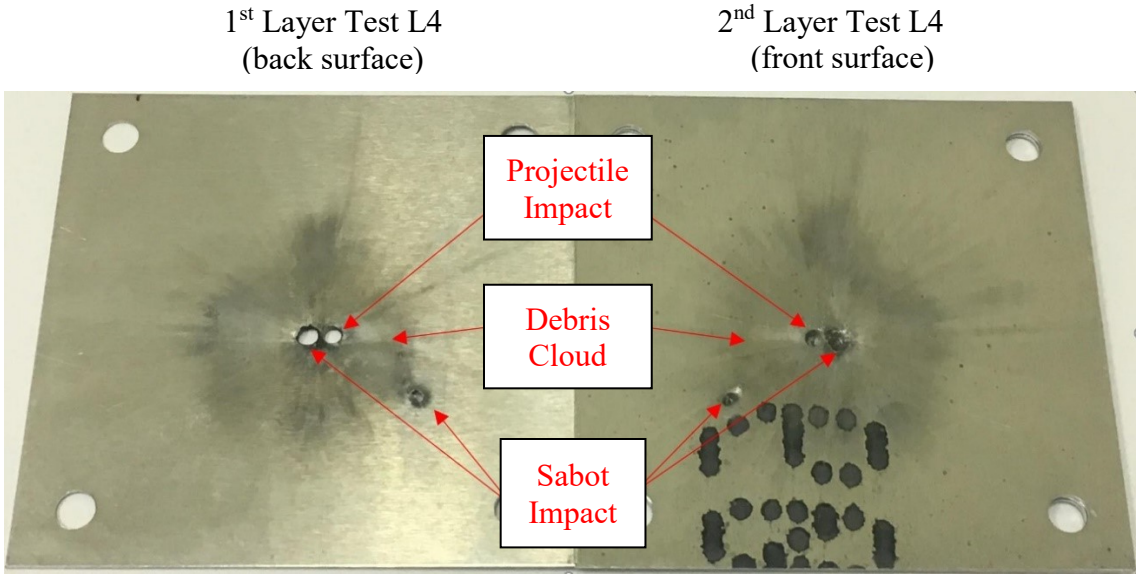

Figure 2.7 Evidence of debris cloud between first (left) and second (right) layer of the four-layer Al 6061-T6 target. The L4 target was impacted by a 1 mm diameter Al 2017-T4 spherical projectile at a velocity of 5.04 km/s.

The layered targets (L1-L4) generally, displayed better HVI penetration resistance than did the monolithic targets (M1-M4). Both targets M4 and L4 were impacted at 5.04 km/s; the monolithic sheet (M4) was completely penetrated by the projectile whereas the innermost layers of target L4 remained. Similarly, when comparing the HVI damage between targets M3 and L3, less HVI damage was observed on the 4-layer target. Evidence of backface cracking was observed in the monolithic target (impact velocity, 4.63 km/s), while a higher impact velocity (4.86 km/s) only produced a back-surface bulge in layered target L3.

2.4 Smoothed Particle Hydrodynamics Estimates of V50

In this work, smoothed particle hydrodynamic (SPH) simulations were performed to predict the ballistic limit of monolithic and layered 6061-T6 targets. SPH numerical

simulations were first developed by Lucy [24] and Gingold and Monaghan [25] for the study of astrophysical and other problems [26]. SPH has since been used to study incompressible flows [27, 28], fracture of brittle solids [29], and HVIs [30, 31].

The smooth particle hydrodynamic code (SPHC) used in this study was developed by Stellingwerf in 1985-1995 [32]. In SPH simulations, a body is idealized as a large system of particles, where each particle carries location, mass, velocity, temperature, and other properties [33]. The SPHC uses a gridless Lagrangian technique that allows particles to move freely relative to one another, an advantage over the traditional finite element method (FEM) [26]. Relative motion between particles is performed by the application of a cubic B-spline smoothing function (kernel) that defines a given particle's range of influence. Particles have a radial range of influence, h or smoothing length (usually proportional to the distance between particles). Hence, the overlapping effect of neighboring particles on the overall influence of a particular particle is readily accounted for [34]. As the particles move in space, the accuracy of the simulation depends on the number of overlapping influences of neighboring particles, and the smoothing length [32].

2.4.1 Material Model and Equation of State

During a HVI, an Al projectile and target both undergo large deformations accompanied by a significant temperature increase. In this study, the Johnson-Cook material model [35] was used to characterize the high strain-rate thermomechanical response of both 2017-T4 projectiles and 6061-T6 targets. The Johnson-Cook flow stress, σ, may be expressed as [32],

$$\sigma = [S_y + B\,(\varepsilon - \varepsilon_y)^n\,]\,[1 + C \ln(d\varepsilon/dt)]\,[1 - (T^*)^m] \qquad (2.1)$$

where S_y, B, n, C, and m are the yield strength, strain hardening constant, hardening exponent, strain rate constant, and thermal softening exponent, respectively. ε, ε_y, $d\varepsilon/dt$ and T^* are the true strain, yield strain, plastic strain rate, and homologous temperature [32]. Here, T^* is defined as,

$$T^* = (T - T_{room}) / (T_{melt} - T_{room}) \quad (2.2)$$

where T, T_{room}, T_{melt} are the current temperature, room temperature and melting temperature, respectively.

Johnson and Holmquist [36] reported the Johnson-Cook material constants for Al 6061-T6, Al 2024-T3, as well as 21 other materials. They did not, however, consider Al 2017-T4. Since Al 2024-T3 has similar material properties to Al 2017-T4, the hardening exponent (n), strain rate constant (C), and thermal softening exponent (m) for Al 2024-T3 were used to approximate those for the Al 2017-T4 projectiles. The strain hardening constant (B) for Al 2017-T4 was calculated by SPHC [32], i.e.,

$$B = (S_u - S_y) / (\varepsilon_{max} - \varepsilon_y)^n \quad (2.3)$$

where S_u, S_y and ε_{max}, are the ultimate tensile strength, yield strength, and maximum extensional strain at fracture for Al 2017-T4, respectively. The Johnson-Cook material constants used for the simulations are given in Table 2.2.

Table 2.2 Johnson-Cook Material Constants for Projectile and Targets

Material Constants	Al 2017-T4 Projectile [32, 36]	Al 6061-T6 Targets [36]
S_y(MPa)	275	324
B(MPa)	252	114
C	0.015	0.002
n	0.34	0.42
m	1.00	1.34

The Mie-Gruneisen equation of state (EOS) [32] is most commonly used for modeling high energy solids and is based on the Rankine-Hugoniot (Hugoniot) relations [37],

$$P = P_h + (\rho\gamma_G)\,(\mathrm{E} - E_h - E_0) \tag{2.4}$$

$$E_0 = (c_v)\,(T_0) \tag{2.5}$$

where P is the pressure, ρ is the current density, γ_G is the Grueneisen gamma, E is the current internal energy, E_0 is the initial internal energy, c_v is the specific heat of the material, and T_0 is the initial temperature. The parameters P_h and E_h may be determined from the Hugoniot relations [32],

$$P_h = K_0\,\eta\,/\,(1 - s\,\eta)^2 \tag{2.6}$$

$$E_h = (1/2)\,P_h\,\eta\,/\,\rho_0 \tag{2.7}$$

where

$$K_0 = \rho_0\,c_s^2 \tag{2.8}$$

$$\eta = 1 - (\rho_0\,/\,\rho) \tag{2.9}$$

Here, ρ_0 is the initial density c_s is the speed of sound of the material, and s is the coefficient of slope of the shock velocity-particle velocity curve. The Mie-Gruneisen EOS is used to account for the sudden change in internal energy (E), pressure (P) and temperature (T) during impact. The EOS (2.5) may be used to calculate the internal energy (E) from the initial temperature (T_0) of the material, and then can be used to determine the pressure and temperature at each timestep. The phase of the material (solid, liquid, vapor, etc.) is determined as a fuction of temperature, and the calculated pressure changes with the phase of the material [32]. The Mie-Gruneisen EOS parameters used in this study [32] are shown in Table 2.3.

Table 2.3 EOS Parameters for Projectile and Target Sheets

Parameter	Al 2017-T4 [32]	Al 6061-T6 [32]
ρ_0 (g/cm^3)	2.79	2.70
c_s (cm/s)	537,587	537,587
c_v (erg/(gK))	8.96 x 10^6	8.80 x 10^6
γ_G	2.1	2.1
s	1.55	1.55

2.4.2 Axisymmetric SPH Models of HVIs to 6061-T6 Monolithic and Layered Targets

Two-dimensional (2D) axisymmetric SPH models were used to simulate 2017-T4 projectile HVIs to monolithic and layered 6061-T6 flat circular targets (diameter, 10.16 cm). Assuming that any projectile penetrations occur prior to stress wave reflections from the target boundaries, use of an axisymmetric idealization gives a reasonable approximation of HVI impacts to square targets with similar dimensions while dramatically reducing the computational run-times. Particle displacements were fixed along the perimeter of the targets, consistent with the experimental tests. Figure 2.8 shows idealizations of the 2017-T4 projectile, monolithic 6061-T6 target, and a four-layer 6061-T6 target in the vicinity of impact. Prior to performing a parametric study investigating the effect of target layering on HVI penetration resistance, a series of validations analyses were performed using experimental and computational results from the literature. As part of each set of SPHC calculations, a particle sensitivity analysis was performed to ensure a converge solution. A given simulation was terminated when the projectile penetrated the target, the target was completely ruptured, or when the average velocity of all projectile particles approached zero (or became negative) while the target remained unruptured.

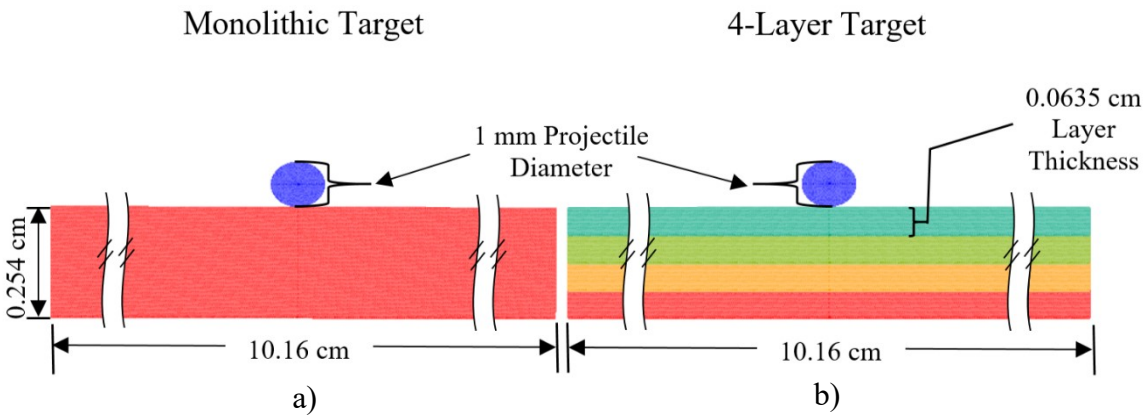

Figure 2.8 SPHC models of a) monolithic target and b) 4-layer target. Projectile and target sheet materials are Al 2017-T4 and Al 6061-T6, respectively.

2.4.3 SPHC Validation

Piekutowski [38] conducted extensive HVI experiments on aluminum bumper sheets and characterized the debris cloud formation using radiographic measurements. For example, Figure 2.9a contains a radiographic image from a 6.71 km/s HVI between a 9.53 mm 2017-T4 projectile and a 152x152x1.5 mm^3 6061-T6 sheet; the image was taken 7.2 μs after impact. The image clearly shows expansion of the debris cloud downstream of the target, as well as ejecta debris upstream of the target. Hayhurst et al. [39] used AUTODYN SPH to predict Piekutowski [38] experimental results. Figure 2.9b shows the predicted debris cloud matches the observed HVI response from [38]. A 2D axisymmetric simulation of Piekutowski's experimental test was performed using SPHC with the material model and EOS previously discussed (Tables 2.2 and 2.3). Figure 2.9c shows the predicted impact behavior 7.2 μs after impact; the simulation captured the essential character of the actual penetration, debris cloud formation, and ejecta and closely matched the predictions of Hayhurst et al. [39] .

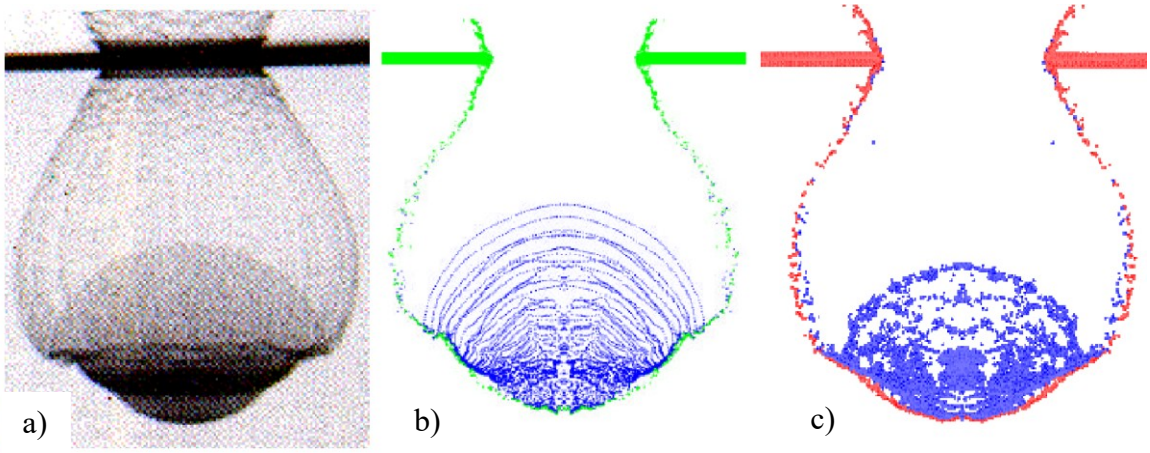

Figure 2.9 HVI response of a 1.5 mm thick Al 6061-T6 sheet 7.2 μs after a 7.6 km/s impact with an Al 2017-T4 projectile; a) Measured radiographic image from [38], b) AUTODYN 2D axisymmetric SPH prediction from [39], and c) 2D axisymmetric SPHC prediction performed in this study.

Roy et al. [40] performed an experimental and numerical study of HVIs on thick metals using the LS-DYNA [14] and CTH [41] hydrocodes. Cylindrical Lexan projectiles (5.6 mm in diameter x 8.6 mm in length) were used to impact ASTM A36 steel target plates (dimensions, 152.4x152.4x12.7 mm^3) at 5.063 km/s. A 2D axisymmetric SPHC simulation was performed and the predicted results were compared to the experimental and LS-DYNA and CTH simulations from [40]. In our simulations, a cylindrical Nylon-6 projectile was used since a complete set of Lexan material properties needed to run SPHC were not available in [40]. Nylon-6 has similar material properties to those of Lexan and is a reasonable substitute material. The same Johnson-Cook material constants and Mie-Gruneisen used by Roy et al. [40] were used in the SPHC simulation. The SPHC model is shown in Figure 2.10.

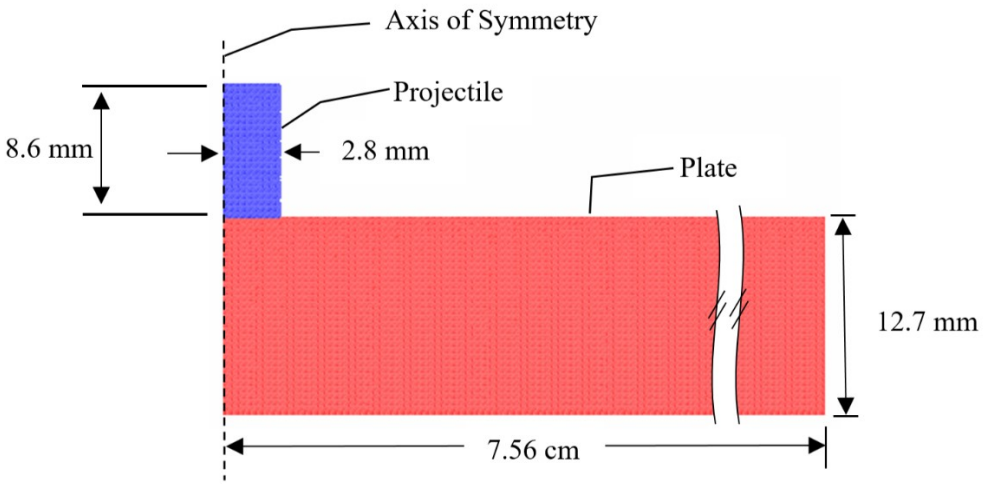

Figure 2.10 2D SPHC model of a cylindrical Nylon-6 projectile and ASTM A36 steel target plate.

Figure 2.11 shows the experimentally observed HVI damage (Figure 2.11a) and predicted damage 10 μs after impact using both LS-DYNA (Figure 2.11b) and CTH (Figure 2.11c) from Roy et al. [40]. The experimental panel (Figure 2.11a) shows significant cratering, backface bulging, and the formation of a well-developed crack lying in the plane of the plate below the impact site; the projectile did not penetrate the target and there was no evidence of spallation. In contrast, the LS-DYNA (Figure 2.11b) and CTH (Figure 2.11c) predictions showed widespread distributed cracking, fragmentation, and some spallation beneath the impact site. No well-developed dominant crack was predicted, but Roy et al. [40] argued that more computational time may be required for cracks to fully develop. Figure 2.11d shows the predicted damage obtained using the SPHC in this study. Consistent with the experimental observations [40] (Figure 2.11a), large-scale cratering, notable backface bulging, and no spallation was predicted. While the SPHC simulation did not predict the formation of a dominant crack (only radial cracking at the point of impact), the predicted crater diameter, crater depth, and backface

bulge all fell within 9% of the measured values from [40]. Table 2.4 contains a summary of these measured and predicted data from [40], as well as the validated SPHC predictions from this study.

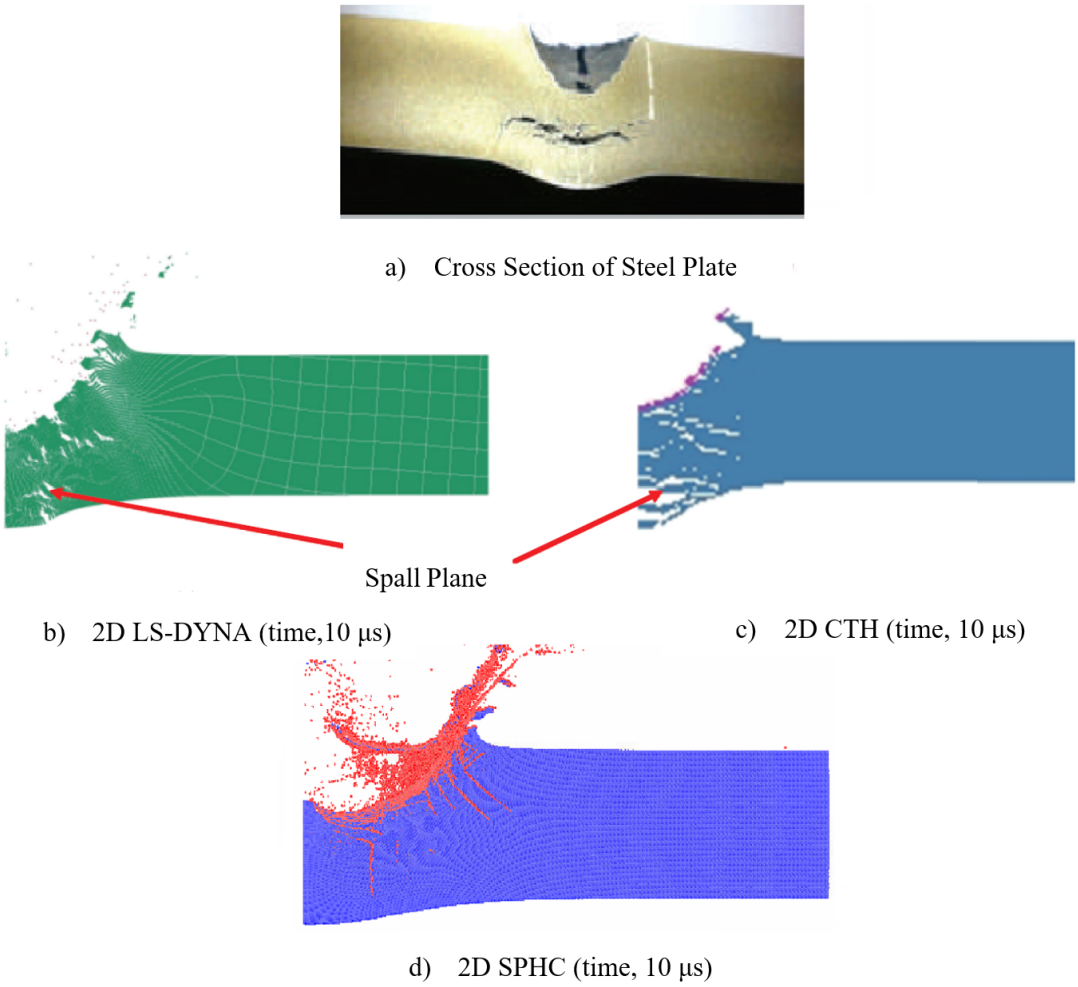

Figure 2.11 HVI damage to a 12.7 mm thick ASTM A36 steel plate due to a 5.6 mm diameter x 8.6 mm Lexan (a, b, and c) or Nylon-6 (d) cylindrical projectile at 5.063 km/s. a) Experimental results from [40]; LS-DYNA (b) and CTH (c) predictions of damage 10 µs after impact from [40]; and SPHC prediction of damage 10 µs after impact in this study.

Table 2.4 Measured [40] and Predicted [40] Hypervelocity Impact Damage to a ASTM A36 Steel Plate due to Plastic Cylinders at a 5.036 km/s Velocity.

Test	Crater Diameter (mm)	Difference (%)	Crater Depth (mm)	Difference (%)	Back Surface Bulge (mm)	Difference (%)
Experimental Test [40]	16.9	N/A	5.8	N/A	2.4	N/A
LS-DYNA [40]	15.9	5.9	5.0	13	2.2	7.8
CTH [40]	15.7	7.1	5.7	1.7	1.9	12.9
SPHC (this study)	18.2	7.7	5.5	5.2	2.2	8.3

2.4.4 SPHC Simulations of HVIs to Monolithic and Layered 6061-T6 Targets

Initial HVI testing of monolithic and layered Al 6061-T6 sheets with the same total thickness showed that the 4-layer target had a higher penetration resistance than a monolithic target for 3.5-5.0 km/s impacts (e.g., Table 2.1). To further explore the effect of layering on HVI ballistic resistance, 2D axisymmetric SPHC models of the 10.16x10.16x0.254 cm^3 6061-T6 monolithic and layered targets subjected to 1 mm diameter Al 2017-T4 projectile impacts were developed. For each target configuration, considered in this study, a particle density sensitivity analysis was conducted in order to ensure a converged solution. A set of simulated impacts to the monolithic sheet were used to establish the predicted ballistic limit, $V50_m \approx 1.25$ km/s. Note that this velocity is somewhat lower than the penetration velocities shown in Table 2.1. Since the ballistic limit is intrinsically a stochastic parameter, numerical predictions of V50 are notoriously difficult. Nonetheless, the SPHC may be used to efficiently probe the *relative* difference in penetration resistance provided by different target layering concepts. SPHC simulations were performed for the monolithic sheet (total thickness, 0.254 cm) and 4-

layer target (sheet thickness, 0.254 cm/4 = 0.0635 cm) subjected to 1.4 km/s projectile impacts. Figure 2.12 contains images of the predicted response for each target at times 0, 10, 20 and 30 μs after impact. The monolithic sheet displayed significant cratering in the vicinity of the impact, accompanied by ejecta of projectile and target fragments away (upstream) from the impact site (Figure 2.12b). Complete penetration occurred within 10 μs after impact. Large plastic deformation occurring through-the-thickness of the sheet led to penetration due to shear plug formation (Figures 2.12b-2.12d). The HVI response of the 4-layer target, however, was profoundly different than for the monolithic plate. 10 μs after impact the projectile completely penetrated the outermost layer, resulting in a significant amount of layer/projectile ejecta and fragmentation accompanied by a substantial separation between the first and second layers (Figure 2.12b). In addition, there was localized plastic deformation (dimpling) occurring directly under the impact site in the second, third, and fourth layers. For the remainder of the impact (10-30 μs; Figure 2.12b-2.12d), the projectile was arrested by the second layer, and slight layer separation was observed between the innermost three layers. A small partial fracture of the second layer was also predicted at the impact site. These results are consistent with numerical simulations of impacts to double-layer shields by Teng et al. [13] where localized penetration of the first layer, large-scale plastic deformation in the second layer, and a significant separation between the layers during impact occurred. Teng et al. [13] characterized the energy dissipation during impact in terms of free surface energy creation (crack initiation) in each layer and inelastic deformation of the second layer. Clearly, complex stress wave interactions between adjacent layers has a dramatic effect on the penetration resistance in a given layered target.

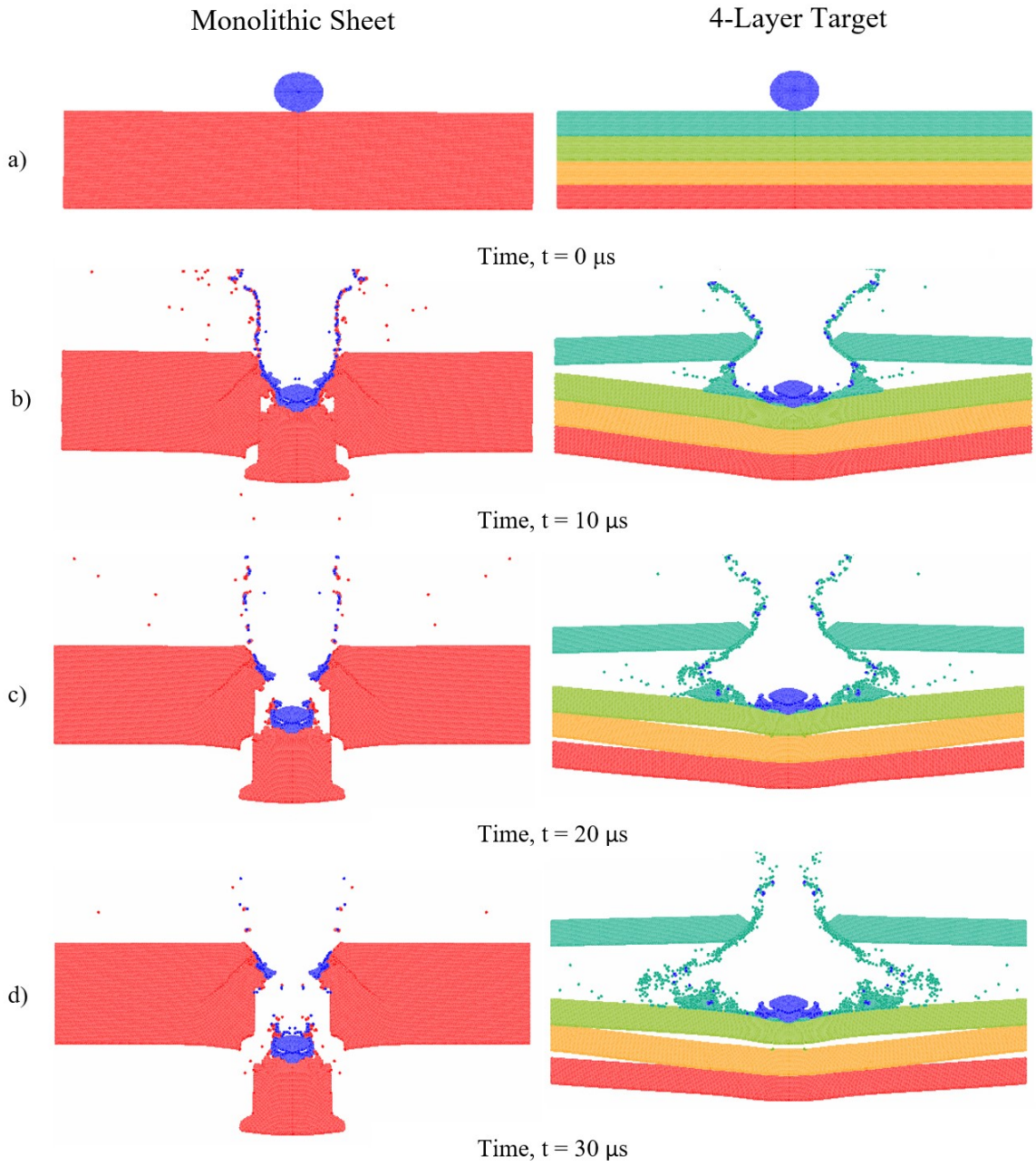

Figure 2.12 HVI response of (left) an Al 6061-T6 monolithic sheet (total thickness, 0.254 cm) and (right) 4-layer target (sheet thickness, 0.254 cm/4 = 0.0635 cm) subjected to 1.4 km/s Al 2017-T4 projectile impacts at a) 0 μs, b) 10 μs c) 20 μs and d) 30 μs after impact.

2.4.4.2 Parametric Study of the Ballistic Limit of Multi-Layered Targets

The preceding numerical simulations suggested that a stack of four Al 6061-T6 sheets displayed better HVI resistance than a monolithic sheet with the same total thickness (0.254 cm). In order to assess the optimum number of thin sheets leading to the maximum penetration resistance for a given target thickness, the SPHC was used to perform a parametric study where 0.254 cm thick targets comprised of 1, 2, 4, 6, 8, 16 and 32 Al 6061-T6 sheets of equal thickness were subjected to HVIs by 1 mm diameter 2017-T4 projectiles. The ballistic limit (V50) for each target was determined, where for purposes of this study V50 is defined as the velocity just *below* that required for complete target penetration (penetration/rapture of every target layer); isolated spallation failure did not constitute penetration of a given layer. As mentioned previously, the complex wave propagation and interaction between adjacent layers strongly influences the penetration of a multi-layered target. In order to properly account for these interactions within a given layer of a layered target, a greater number of particles is required than for a monolithic target. As a consequence, SPHC models for predicting V50 were developed for each 1-, 2-, 4-, 6-, and 8-layer target using 50k, 100k, 200k, 300k, 400k, and 500k total particles. In general, the predicted V50 decreased with an increasing number of particles. For example, Figure 2.13 contains a plot of the ballistic limit for the monolithic target and 2-, 4-, 6-, and 8-layer targets as a function of the total number of particles in a given simulation. The calculated V50 for the monolithic plate steadily decreased with increasing number of particles, and asymptotically approached a constant value once the number of particles exceeded 200k. The solutions for each of the multi-layer targets also

tended to converge with increasing particle density, but the total number of particles required for a converged solution generally increased as the number of layers increased. Converged V50 solutions for 16- and 32-layer targets were not possible since the total number of particles required (>10^6) was computationally intractable.

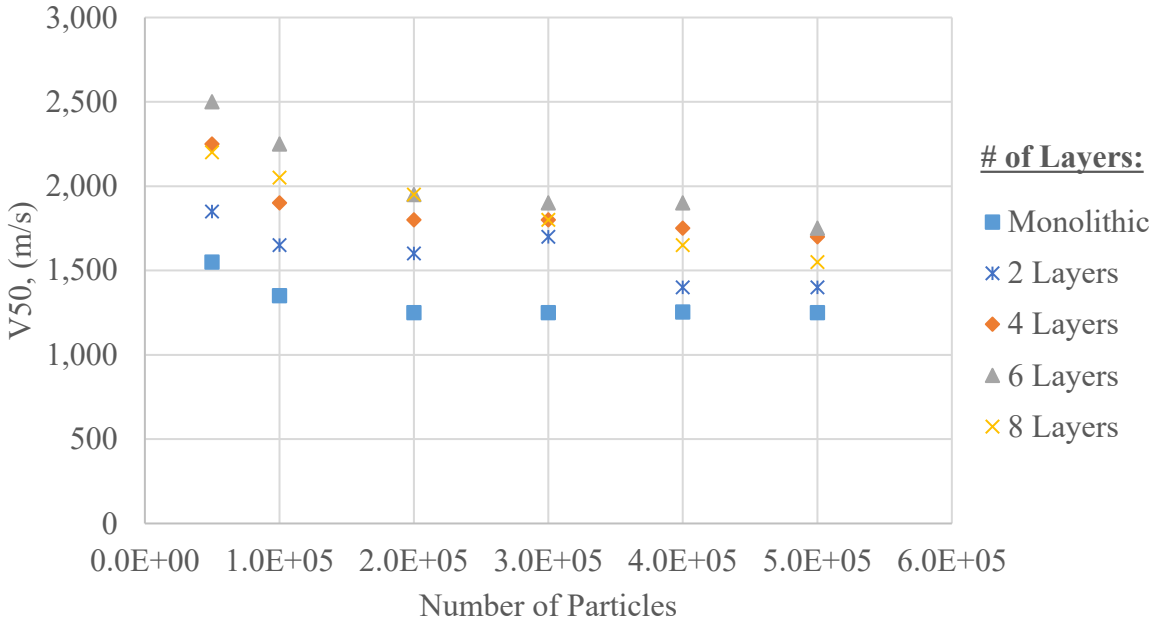

Figure 2.13 Ballistic limit (V50) upon increasing particle density (50k, 100k, 200k, 300k, 400k, and 500k) for the Al 6061-T6 monolithic target and the 2-, 4-, 6-, and 8-layer targets subjected to 1 mm diameter Al 2017-T4 projectiles. A constant total thickness 0.254 cm was held on all predicted V50 simulations.

Based upon the parametric study, the predicted ballistic limit increased as the number of layers in a given target was increased from 1-6; any further increase in the number of layers led to a *decrease* in the predicted V50. Figure 2.14 contains a plot in the predicted V50 as a function of the number of target layers. For simulations performed using 500k particles, increasing the number of layers from 1-6 led to roughly a 40%

increase in V50. Interestingly, simulations performed using less particles also were able to capture the *relative* improvements in V50 for layered targets (although the magnitude of the individual values maybe somewhat high). The initial beneficial effect associated with increasing the number of Al 6061-T6 sheets is likely due to increased impact energy dissipation associated with the presence of multiple free surfaces throughout the target stack-up; the nature of the transmitted/reflected stress waves in each layer are no doubt influenced by the lack of adhesion between layers. In addition, dominant flaws initiated in one layer cannot readily propagate into adjacent layers; the energy required to initiate and propagate new flaws in an underlying layer is likely higher than that required to propagate large flaws in a monolithic target. As the thickness of a given layer decreases, however, the layer becomes increasingly prone to penetration/fragmentation during impact. Such a tendency may eventually outweigh the beneficial effects of multi-layering. This may explain the reduction in V50 once the layer thickness falls below 1/8 of the total target thickness.

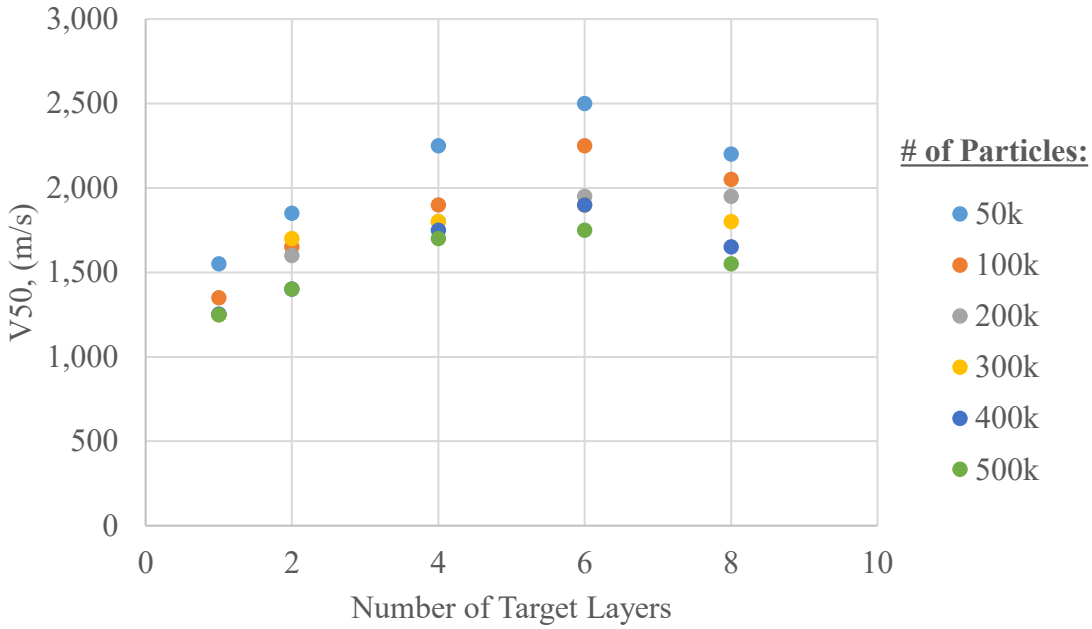

Figure 2.14 Ballistic limit (V50) upon increasing the number of Al 6061-T6 target layers subjected to 1 mm diameter Al 2017-T4 projectile impacts. The predicted V50 was performed using 50k, 100k, 200k, 300k, 400k and 500k total particles.

Figure 2.15 presents a plot of the normalized ballistic limit for each target ($V50/V50_m$) considered in this study, where $V50_m$ is the predicted ballistic limit for the monolithic (single-layer) target. 500k particles were used in the simulations of 1-, 2-, 4-, 6-, and 8-layer targets. 100k and 300k particles were used in the analysis of the 16- and 32- layer targets. Hence, the calculated V50 values for these targets would be somewhat lower if more particles were used in the simulations; a downward pointing arrow is included with the data in Figure 2.15 to indicate the converged values would likely be lower than those shown in the figure. As can be seen in the figure, 2-, 4- and 6-layer targets showed a relative 12%, 36%, and 40% improvement in ballistic resistance compared to the monolithic sheet. Further increases in the number of sheets reduced the relative advantage of layering, where eventually a 32-layer target had a predicted ballistic

limit *lower* than the monolithic sheet. Nevertheless, Figure 2.15 underscores the beneficial effects of subdividing a homogenous target into a number of discrete separate layers of equal thickness. As an aside, Marom and Bodner [17] concluded a layer thickness corresponding to 1/3 of the target thickness provided the optimal penetration resistance for impacts (averaging 375 m/s) to 6061-T6 targets. In the future, highly tailored targets maybe developed involving combinations of hard/soft layers with designed interfaces to further enhance ballistic resistance. This is the topic of ongoing research at MSU.

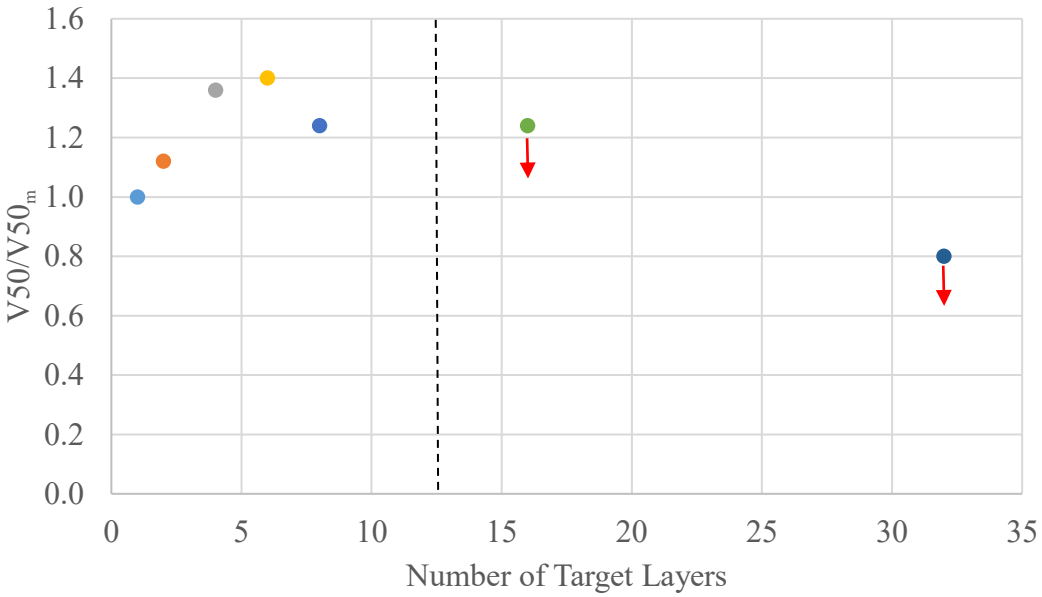

Figure 2.15 Normalized ballistic limit ($V50/V50_m$) upon increasing number of equally thick layers at constant total thickness of 0.254 cm. In all predicted V50 simulations, an Al 2017-T4 projectile impacted an Al 6061-T6 target. Overestimated V50 is shown past the vertical dash line; downward arrows indicate the V50 to be lower than what is shown.

As mentioned previously, the presence of distinct target layers inhibits the propagation of larger dominant flaws through the entire target thickness. In general,

increasing the number of layers can *inhibit* or *accelerate* operative damage mechanisms relative to those for a monolithic sheet of the same total thickness. For example, Figures 2.16a and 2.16b show the HVI response of 4- and 16-sheet targets, respectively, at a time, 10 μs, after a 1.4 km/s impact; 500k particles were used in each simulation. Recall that a monolithic target predicted ($V50_m \approx 1.25$ km/s) failed due to shear plugging when impacted at 1.4 km/s (Figure 2.12). Both the 4- and 16-layer targets displayed projectile/target fragmentation, substantial separation between layers, and inelastic dimpling directly beneath the impact site. For the 4-layer target, the projectile penetrated one sheet (i.e., ¼ of the total thickness) and caused a small fracture in the second layer. In contrast, the projectile penetrated the first five layers in the 16-layer target (5/16 of the total thickness) and resulted in partial facture of the underlying 6^{th} layer. Moreover, spallation-like fracture of the 14-16^{th} layers occurred. Clearly, the 16-layer target displayed lower penetration resistance than the 4-layer target. As mentioned previously, the 32-layer target had a lower predicted V50 than did a monolithic sheet of the same thickness. This underscores the importance of characterizing the relevant failure mechanisms associated with increasing number of target layers.

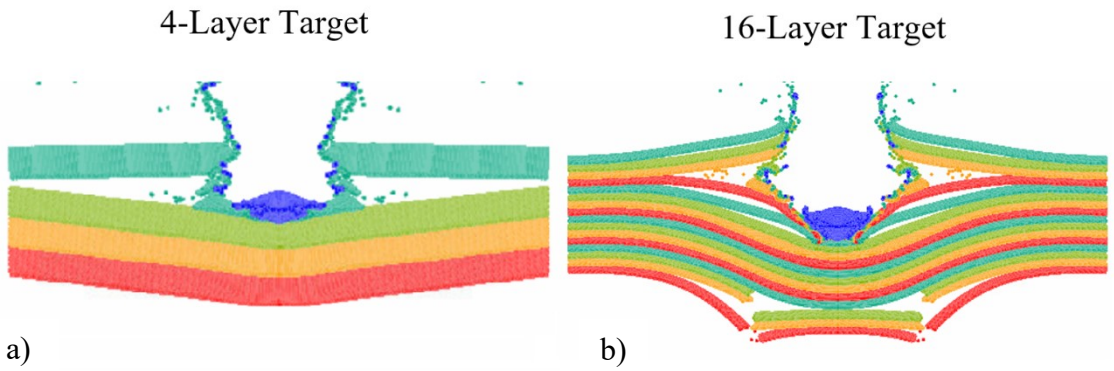

Figure 2.16 Comparison of Al 6061-T6 a) 4-layer target to b) 16-layer target subjected to a 1 mm diameter Al 2017-T4 projectile HVI of 1.4 km/s at 10 μs after impact. A total target thickness of 0.254 cm was used for both simulations.

2.4.4.3 Effect of Variable Target Layer Thicknesses on Penetration Resistance

The previous simulations demonstrated the relative improvement in predicted V50 associated with homogeneous targets comprised of discrete layered sheets of constant thickness. An alternative strategy would be to construct layered targets with sheets of *variable* thickness. For example, a 0.254 cm thick Al 6061-T6 3-layer target could consist of two 0.0635 cm thick outer sheets stacked upon a 0.127 cm thick inner sheet, where each sheet comprises ¼, ¼, and ½ of the total target thickness, respectively. For convenience, this target configuration can be identified as [¼ / ¼ / ½] or simply [$(¼)_2$ / ½] (cf. Figure 2.17a). If the thicker 0.127 cm sheet was repositioned as the outermost layer in the 3-layer target, the new configuration would be defined as simply [½ / $(¼)_2$] (cf., Figure 2.17b).

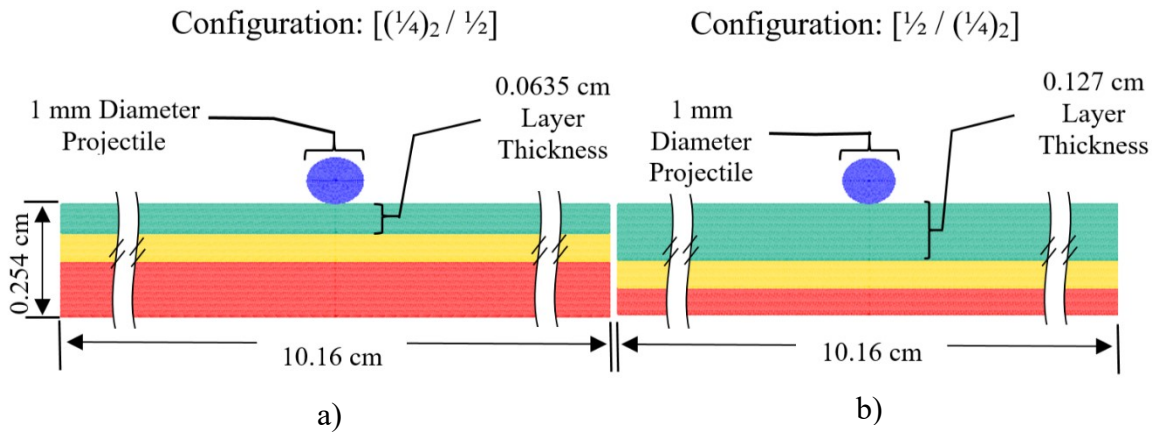

Figure 2.17 SPHC models for a) [(¼)2 / ½] and b) [½ / (¼)2] target configurations. Projectile and target sheet materials are Al 2017-T4 and Al 6061-T6, respectively.

The SPHC was used to simulate 1 mm diameter AL 2017-T4 projectile impacts to 0.254 cm thick 6061-T6 layered targets comprised of sheets of variable thickness. In the analysis, a total of 200k particles were used to simulate each ¼ layer and 400k particles for ½ layer. For example, Figure 2.18 shows the predicted response of [(¼)2 / ½] and [½ / (¼)2] targets 10 μs after a 1.4 km/s projectile impact. Included in the figures is an image of a monolithic sheet subjected to the same impact (total number of particles, 800k). Neither of the layered targets were penetrated by the projectile; the single-layer sheet, however, failed due to shear plug formation (Figure 2.18c). For the layered targets, concentrating the thinner 0.0635 cm sheets on the outside of the target led to less predicted impact damage. For the [(¼)2 / ½] configuration (Figure 2.18a), the projectile only penetrated *one-fourth* of the way through the target. There was substantial fracture/fragmentation of the projectile and outmost 0.0635 cm thick sheet, accompanied by a significant separation between the first two sheets. The underlying 0.0635 cm and 0.127 cm sheets experienced inelastic dimpling beneath the impact site but otherwise remained intact. For the [½ / (¼)2] target, however, the projectile penetrated *one-half* of

the target thickness. The 0.127 cm thick outer sheet failed due to shear plug formation. There was separation of the second and third layers from the first layer, along with a higher degree of plastic deformation in the innermost two layers. For the given 3-layer targets, locating the relatively thinner sheets on the impact side led to improved penetration resistance. This may be due to better shock wave interaction and dispersion associated with the presence of free surfaces between layers, as well the inability of dominant flaws in one layer to propagate through the thickness.

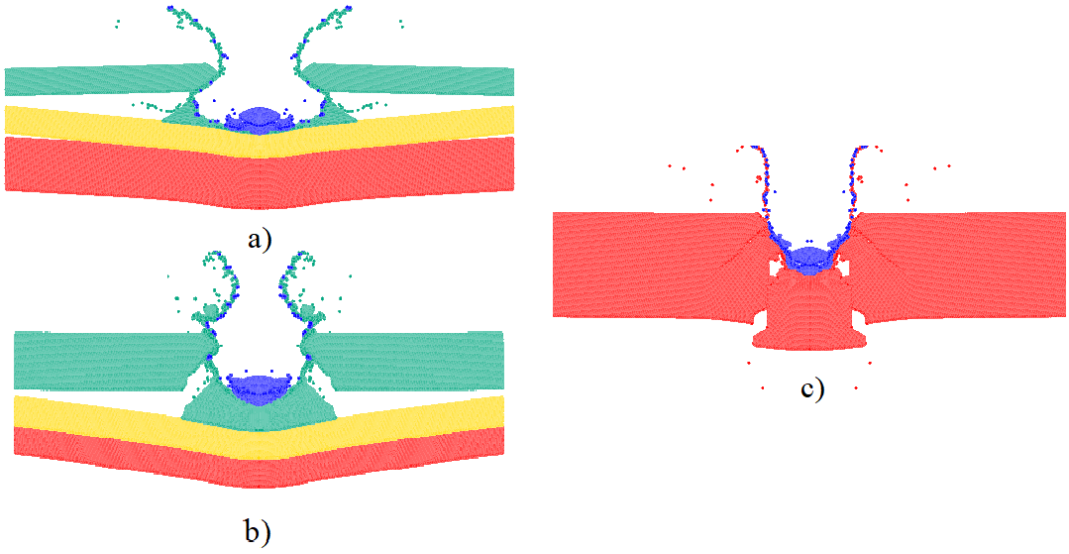

Figure 2.18 Predicted HVI response of Al 6061-T6 a) [(¼)$_2$ / ½], b) [½ / (¼)$_2$] and c) monolithic sheet target subjected to 1 mm diameter 2017-T4 projectile HVI of 1.4 km/s at 10 μs after impact. A constant target total thickness of 0.254 cm was held in all three simulations.

A similar set of simulations were performed for the two 3-layer targets and a 4-layer target comprised of sheets of equal layer thickness, i.e., [(¼)$_4$]. The targets were subjected to simulated impacts at 1.6 km/s. Figure 2.19 shows the predicted response of each target 10 μs after impact. Both of the 3-layers targets were penetrated at this impact

velocity. The [(¼)$_2$ / ½] target experienced large-scale fragmentation of the projectile and outermost layer, as well as outer layer separation (Figure 2.19a). The second 0.0635 cm thick layer and third 0.127 cm thick layer both failed due to large plastic deformation and shear plug formation. The nature of the failure mechanisms in each layer was different for the second [½ / (¼)$_2$] target (Figure 2.19b) than for the first [(¼)$_2$ / ½] 3-layer target. The outermost 0.127 cm thick layer failed primarily due to shear plug formation along with projectile/sheet fragmentation (Figure 2.19b). The underlying 0.0635 cm thick layers experienced inelastic dimpling that extended well beyond the region directly under the impact site. These layers failed due to the formation of slant cracks roughly several projectile diameters outside of the line of impact. The 4-layer target with uniform sheet thickness (Figure 2.19c) was not penetrated by the projectile. The outermost sheet fragmented during impact, and the remaining three sheets underwent widespread inelastic deformation and dimpling. Interestingly, the third sheet failed due to slant crack formation away from the line of impact. There was a slight separation between the third layer and the adjacent two layers, but the second and fourth layer each remained intact.

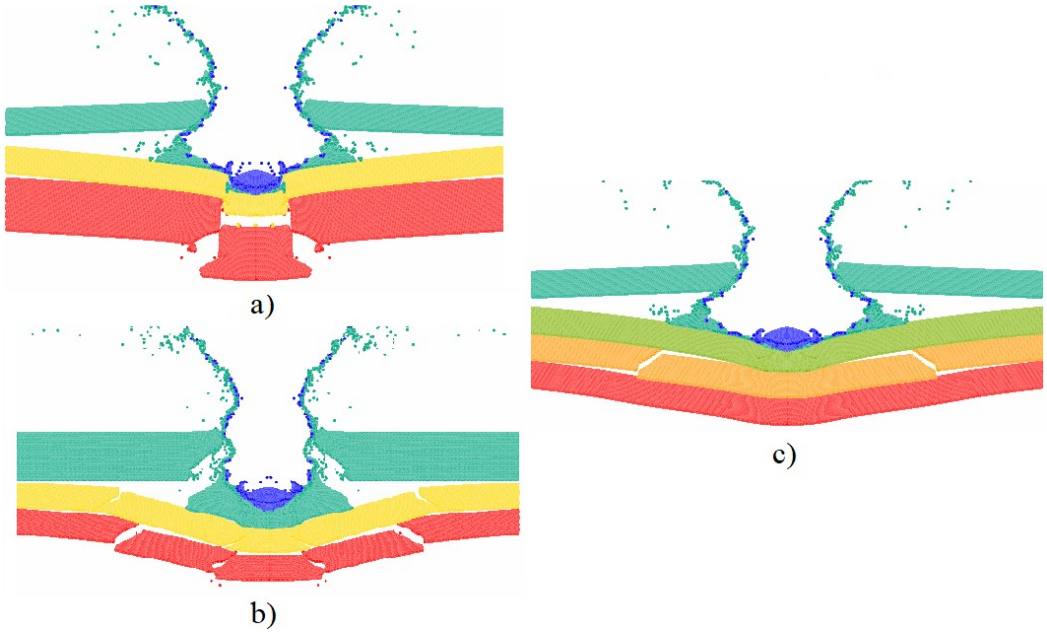

Figure 2.19 Predicted HVI response of Al 6061-T6 a) [(¼)$_2$ / ½], b) [½ / (¼)$_2$] and c) 4-layer target subjected to 1 mm diameter 2017-T4 projectile HVI of 1.6 km/s at 10 μs after impact. A constant target total thickness of 0.254 cm was held in all three simulations.

Positioning two relatively thin sheets on the impact side of a 3-layer target provided better penetration resistance than for a monolithic sheet of the same total thickness, but not as great as that for a 4-layer target with uniform sheet thicknesses [(¼)$_4$]. In order to further assess the effect of positioning multiple thin sheets on the impact side of a homogenous target, an additional 1.60 km/s HVI simulation was performed for a 5-layer target comprised of four 0.0317 cm thick layers stacked upon an inner 0.127 cm thick layer, [(1/8)$_4$ / ½]. Figure 2.20 shows the predicted response of the target 10 μs after impact. In contrast to the [(¼)$_2$ / ½] target (Figure 2.19a), the 5-layer target was not penetrated by the projectile. The target displayed typical fragmentation/fracture of the two thin outer layers along with large inelastic deformation and fracture of the last three sheets (layers 3, 4, and 5); the predicted impact response suggests the 5-layer target is approaching its ballistic limit. Clearly, the number,

thickness, and arrangement of sheets in a layered target has a profound effect on penetration resistance.

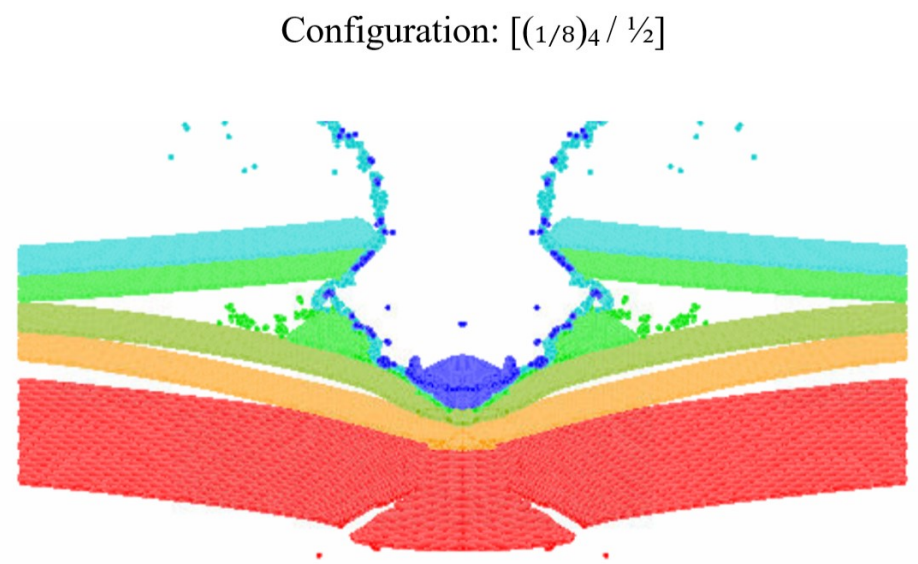

Figure 2.20 HVI impact response of Al 6061-T6 [(1/8)4 / ½] target subjected to 1 mm diameter Al 2017-T4 projectile at a HVI of 1.60 km/s at 10 μs after impact with a total thickness of 0.254 cm.

Figure 2.21 contains a plot of the predicted normalized ballistic limit ($V50/V50_m$) for the 1-, 2-, 4-, 6-, 8-, 16- and 32-layer targets comprised of discrete sheets of constant thickness. Included in the chart is the predicted ($V50/V50_m$) for the three targets with variable sheet thickness, [(¼)2 / ½], [½ / (¼)2] and [(1/8)4 / ½]. For the range targets considered, the 6-layer target provided the best overall penetration resistance. Positioning thin layers on the impact side of the target appeared to provide a modest improvement in the impact resistance. While most of the layered targets had a higher predicted ballistic limit than did a monolithic target with the same total thickness, use of a large number of excessively thin layers may result in a *decrease* in penetration resistance. Nonetheless, this study indicates that simple changes in target geometries can have a profound effect

on HVI resistance. In the future, this work can be extended to include hard/soft layers with tailored interfaces that aim to maximize the energy dissipated associated with a given impact.

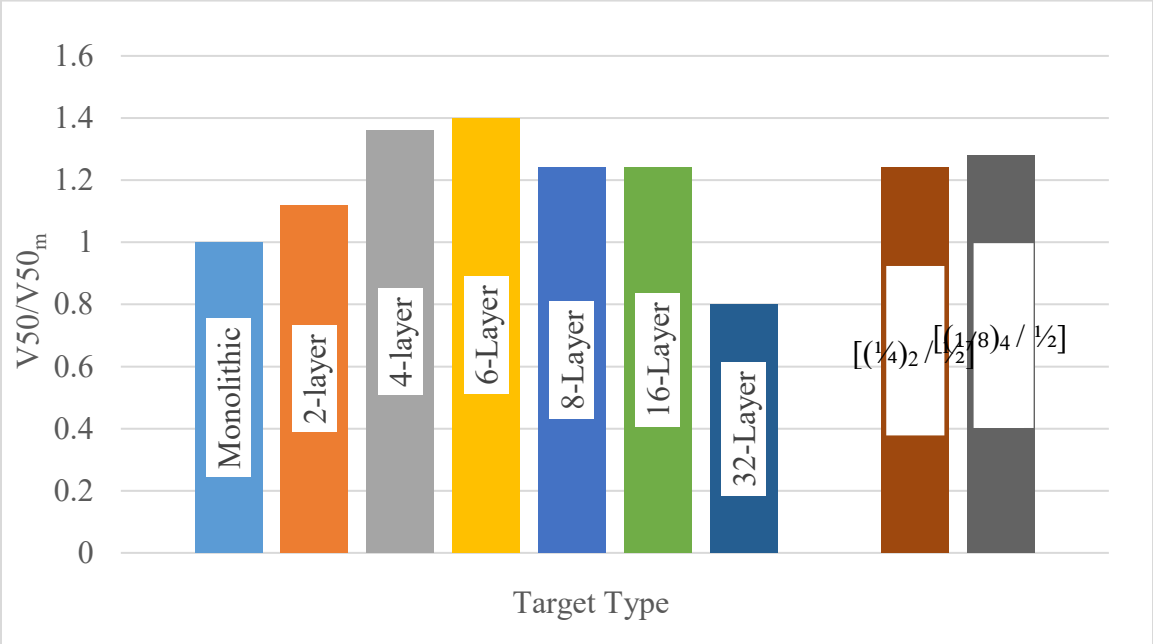

Figure 2.21 Normalized ballistic limit ($V50/V50_m$) comparison between multi-layer targets of equally thick layers versus targets of varying layer thickness. For all predicted V50 simulations, a 1 mm diameter Al 2017-T4 projectile impacted an Al 6061-T6 target with a total thickness of 0.254 cm.

2.5 Conclusions

In this study, smooth particle hydrodynamic simulations were used to assess the relative improvement in penetration resistance of 0.254 cm thick homogenous Al 6061-T6 targets comprised of discrete layered sheets of constant thickness, as well as similar targets constructed using variable thickness sheets. The simulated targets were subjected to hypervelocity impacts (HVIs) with 1mm diameter spherical Al 2017-T4 projectiles. In general, the penetration resistance of the target initially increased as the number of

stacked layers of constant thickness was increased from one to six. The estimated ballistic limit for a 6-layer target was roughly 40% greater than for a monolithic target with the same overall thickness. As the number of constant thickness layers in a given target was further increased, the penetration resistance *decreased*. For targets comprised of large numbers of exceedingly thin sheets, the ballistic limit of a given target may fall *below* that for a monolithic sheet with the same total thickness. For targets containing a number of stacked sheets of variable thickness, positioning thinner sheets on the impact side of the target appears to provide a modest improvement in penetration resistance compared to the case where such layers are located on the backside of the target. Also, the sequence of operative failure mechanisms can change as the number of stacked target layers increases.

The relative improvement in HVI penetration resistance associated with some simple layered target geometries may be due to enhanced shock wave attenuation and dispersion due to the presence of free surfaces between layers. In addition, dominant flaws that initiate and grow in one layer cannot propagate into adjacent layers. The free surface energy released during fragmentation/cracking for several target geometries is likely greater than for a monolithic target subjected to an identical impact.

In the future, multi-layered targets comprised of alternating layers of hard and soft materials with tailored interfaces will be developed, tested and analyzed in an attempt to fully exploit the maximum energy absorption capability of judiciously selected material/geometry combinations. State-of-the-art HVI testing is now possible using the newly established HVI Laboratory at Mississippi State University.

CHAPTER III

CONCLUSIONS AND FUTURE WORK

3.1 Conclusions

Protection against orbital debris has been a major topic area in spaceflight over the last decade. Different space shields (monolithic shield, Whipple Shield, Stuffed Whipple Shield, etc.) are currently being implemented, however, little research is available on the optimization of space shields by subdividing a monolithic wall into multiple adjacent layers with the same total thickness. In this thesis, preliminary HVI testing showed a stack of four Al 6061-T6 sheets had a higher penetration resistance than a monolithic sheet when subjected to 1 mm dimeter Al 2017-T4 projectile HVIs at a constant total thickness of 0.254 cm. To further assess the effects of multi-layering, a parametric study was performed using 2D axisymmetric SPH simulations to demonstrate the *relative* differences in penetration resistance between a monolithic sheet and targets comprised of 2, 4, 6, 8, 16 and 32 sheets of equal layer thickness while maintaining the same overall thickness (0.254 cm). The study predicted an increase in the ballistic resistance from 1-6 layers by 40%; further increases in the number of layers decreased the ballistic resistance, where eventually a 32-layer target had a V50 lower than the monolithic sheet. The initial increase in the ballistic resistance maybe associated with the energy dissipation when dominate flaws initiated in one layer are inhibited from propagating into adjacent layers; the energy required to initiate and propagate new flaws

in an underlying layer is likely higher than that required to propagate large flaws in a monolithic target. The energy dissipation may also be related to stress wave interaction and dispersion associated with presence of free surfaces between layers and inelastic deformation of the layered sheets. As the number of targets exceed six, the decline in the ballistic resistance is related to the decrease in penetration resistance of individual layers. Once the layer thickness falls to 1/8 of the total target thickness or lower, the layer becomes increasingly prone to penetration/fragmentation during impact. Such a tendency eventually outweighs the beneficial effects of multi-layering.

The concept of varying layer thicknesses in a multi-layer target was also considered in this thesis. Positioning a set of relative thin layers in front of a thicker layer led to a modest increase in the penetration resistance compared to the inverse configuration. However, varying the layer thickness in a target did not drastically increase the penetration resistance compared to multi-layered targets of equal layer thicknesses. Nevertheless, this study showed that such simple changes in the target geometry has an impact on the penetration resistance.

Note that the relative differences in penetration resistance discussed in this work will vary with projectile velocity, ratio of the projectile diameter to target thickness, and projectile shape. Nevertheless, this thesis demonstrates an increase in the performance of advanced space shielding structures maybe be possible using multi-layering concepts. By applying a multi-layered structure on the interior thick wall of a Whipple Shield or Stuffed Whipple Shield, further increases in the ballistic resistance may be realized without an increase in the structural mass. It also suggests that it may be possible to

dramatically improve the performance of such structures by tailoring the material properties, interfaces, and layering concepts.

3.2 Future Work

In this thesis, the material of the target and projectile, as well as the total thickness of the target, were held constant. With our new state-of-the-art HVI testing capabilities established at Mississippi State University, large scale highly tailored targets may be developed involving combinations of hard/soft layers with designed interfaces to further enhance ballistic resistance.

REFERENCES

[1] M. Garcia, "Space Debris and Human Spacecraft," NASA, September 2013. [Online]. Available: URL:http://www.nasa.gov/mission_pages/station/news/orbital_debris.html#.VKxr6CvF9qU. [Accessed January 2017].

[2] D. Shoots and P. Anz-Meador, Eds."Orbital Debris Quaterly News," *NASA Orbital Debris Program,* vol. 21, no. 1, p. 12, February 2017.

[3] T. S. Kelso, "Analysis of the 2007 Chinese ASAT Test and the Impact of its Debris on the Space Environment," in *Advanced Maui Optical and Space Surveillance Technologies Conference*, Maui, Hawaii, 2007.

[4] L. Anselmo and C. Pardini, "Analysis of the Consequences in Low Earth Orbit of the Collision between Cosmos 2251 and Iridium 33," in *21st International Symposium on Space Flight Dynamics*, Toulouse, France, 2009.

[5] "Hypervelocity Impact Technology," NASA, [Online]. Available: https://ares.jsc.nasa.gov/orbital_debris/hvit/impact-galleries/shuttle-impact-gallery.html. [Accessed April 2017].

[6] F. L. Whipple, "Meteorites and Space Travel," *The Astronomical Journal,* vol. 52, p. 131, 1947.

[7] E. L. Christiansen, J. L. Crews, J. E. Williamsen, J. H. Robinson and A. M. Nolen, "Enhanced Meteoroid and Orbital Debris Shielding," *International Journal of Impact Engineering,* vol. 17, no. 1-3, pp. 217-228, 1995.

[8] A. J. Mateos, "Space Debris and Its Effects on Spacecrafts," 2009. [Online]. Available: http://www.its.caltech.edu/~ajmateos/Documents/Extended_Essay_Arturo_Mateos_2009.pdf. [Accessed May 2017].

[9] "Technical Standards," 2008. [Online]. Available: https://standards.nasa.gov/standard/nasa/nasa-hdbk-871914. [Accessed April 2017].

[10] E. L. Christiansen, "Design and Performance Equations for Advanced Meteoroid and Debris Shields," *International Journal of Impact Engineering,* vol. 14, no. 1-4, pp. 145-156, 1993.

[11] E. L. Christiansen and J. H. Kerr, "Mesh Double-Bumper Shield: A Low-Weight Alternative for Spacecraft Meteoroid and Orbital Debris Protection," *International Journal of Impact Engineering,* vol. 14, no. 1-4, pp. 169-180, 1993.

[12] B. G. Cour-Palais and J. L. Crews, "A Multi-Shock Concept for Spacecraft Shielding," *International Journal of Impact Engineering,* vol. 10, no. 1-4, pp. 135-146, 1990.

[13] X. Teng, S. Dey, T. Børvik and T. Wierzbicki, "Protection Performance of Double-Layered Metal Shields Against Projectile Impact," *Journal of Meachanics of Materials and Structures,* vol. 2, no. 7, pp. 1309-1329, 2007.

[14] "Download/Order LSTC Product Manuals," Livermore Software Technology Corporation, [Online]. Available: http://www.lstc.com/download/manuals. [Accessed July 2017].

[15] S. Dey, T. Børvik, X. Teng, T. Wierzbicki and O. S. Hopperstad, "On the Ballistic Resistance of Double-Layered Steel Plates: An Experimental and Numerical Investigation," *International Journal of Solids and Structures ,* vol. 44, no. 20, pp. 6701-6723, 2007.

[16] T. Børvik, S. Dey and A. H. Clausen, "A Preliminary Study on the Perforation Resistance of High-Strength Steel Plates," *Journal de Physique IV (France),* vol. 134, pp. 1053-1059, 2006.

[17] I. Marom and S. R. Bodner, "Projectile Perforation of Multi-Layered Beams," *International Journal of Mechanical Sciences ,* vol. 21, no. 8, pp. 489-504, 1979.

[18] R. M. Gamache, C. B. Giller, G. Montella, D. Fragiadakis and C. M. Roland, "Elastomer-Metal Laminate Armor," *Materials and Design,* vol. 111, pp. 362-368, 2016.

[19] J. Randi and W. Goldsmith, "Normal Projectile Penetration and Perforation of Layered Targets," *International Journal of Impact Engineering,* vol. 7, no. 2, pp. 229-259, 1988.

[20] A. A. Almohandes, M. S. Abdel-Kader and A. M. Eleiche, "Experimental Investigation of the Ballistic Resistance of Steel-Fiberglass Reinforced Polyester Laminated Plates," *Composites Part B: Engineering,* vol. 27, no. 5, pp. 447-458, 1996.

[21] G. Ben-Dor, A. Dubinsky and T. Elperin, "New Results on Ballistic Performance of Multi-Layered Metal Shields: Review," *Theoretical and Applied Fracture Mechanics ,* vol. 88, pp. 1-8, 2017.

[22] B. A. Hardage and F. C. Todd, "Design and Construction of a Helium Gas Gun for Hypervelocity Impact," *Oklahoma Academy of Science,* vol. 45, pp. 129-138, 1965.

[23] S. Sen, E. Schofield, J. S. O'Dell, L. Deka and S. Pillay, "The Development of Multifunctional Composite Material for Use in Human Space Exploration Beyond Low-Earth Orbit," *JOM: The Journal of the Minerals, Metals & Materials Society,* vol. 61, no. 1, pp. 23-31, 2009.

[24] L. B. Lucy, "A Numerical Approach to the Testing of the Fission Hypothesis," *Astronomical Journal,* vol. 82, pp. 1013-1024, 1977.

[25] R. A. Gingold and J. J. Monaghan, "Smoothed Particle Hydrodynamics- Theory and Application to Non-Spherical Stars," *Monthly Notices of the Royal Astronomical Society ,* vol. 181, pp. 375-389, 1977.

[26] G. R. Liu and M. B. Liu, Smoothed Particle Hydrodynamics: A Meshfree Particle Method, Hackensack, NJ: World Scientific Publishing Company, Incorporated, 2003.

[27] J. J. Monaghan, "Simulating Free Surface Flows with SPH," *Journal of Computational Physics,* vol. 110, no. 2, pp. 399-406, 1994.

[28] J. P. Morris, P. J. Fox and Y. Zhu, "Modeling Low Reynolds Number Incompressible Flows Using SPH," *Journal of Computational Physics,* vol. 136, no. 1, pp. 214-226, 1997.

[29] W. Benz and E. Asphaug, "Simulations of Brittle Solids Using Smooth Particle Hydrodynamics," *Computer Phusics Communications,* vol. 87, no. 1-2, pp. 253-265, 1995.

[30] C. J. Hayhurst and R. A. Clegg, "Cylindrically Symmetric SPH Simulations of Hypervelocity Impacts on Thin Plates," *International Journal of Impact Engineering,* vol. 20, no. 1-5, pp. 337-348, 1997.

[31] L. D. Libersky, P. W. Randles, T. C. Carney and D. L. Dickinson, "Recent Improvements in SPH Modeling of Hypervelocity Impact," *International Journal of Impact Engineering,* vol. 20, no. 6-10, pp. 525-532, 1997.

[32] R. F. Stellingwerf, "SPHC Smoothed Particle Hydrodynamics Code User Guide," Stellingwerf Consulting, Huntsville, Al, 2014.

[33] C. E. Knapp, "An Implicit Smooth Particle Hydrodynamic Code," Los Alamos National Laboratory, Albuquerque, NM, 2000.

[34] A. Thurber and J. Bayandor, "On the Fluidic Response of Structures in Hypervelociy Impacts," *Journal of Fluids Engineering,* vol. 137, no. 4, 2015.

[35] G. R. Johnson and E. Cook, "A Constitutive Model and Data for Metals Subjected to Large Strains, High Strain Rates and High Temperatures," in *7th International Symposium on Ballistics*, The Hauge, South Holland, The Neatherlands, 1983.

[36] G. R. Johnson and T. J. Holmquist, "Test Data and Computational Strength and Fracture Model Constants for 23 Materials Subjected to Large Strains, High Strain Rates, and High Temperatures," Los Almos National Laboratory, Los Almos, NM, 1989.

[37] B. M. Corbett, "Numerical Simulations of Target Hole Diameters for Hypervelocity Impacts into Elevated and Room Temperature Bumpers," *International Journal of Impact Engineering,* vol. 33, no. 1-12, pp. 431-440, 2006.

[38] A. J. Piekutowski, "Formation and Description of Debris Clouds Produced by Hypervelocity Impact," NASA Contractor Report 4707, Huntsville, AL, 1996.

[39] J. C. Hayhurst, I. H. Livingstone, A. R. Clegg and G. E. Fairlin, "Numerical Simulation of Hypervelocity Impacts on Aluminum and Nextel/Kevlar Whipple Shields," in *Hypervelocity Shielding Workshop*, Galveston, TX, 1998.

[40] K. S. Roy, M. Trabia, B. O'Toole, R. Hixson, S. Becker, M. Pena, R. Jennings, D. Somasoundaram, M. Matthes, E. Daykin and E. Machorro, "Study of Hypervelocity Projectile Impact on Thick Metal Plates," *Shock and Vibration,* p. 11, 2016.

[41] "CTH Shock Physics," Sandia National Laboratories, [Online]. Available: http://www.sandia.gov/CTH/index.html. [Accessed July 2017].